DEVELOPMENT OF MONOLITHIC CERAMICS AND HIGH-TEMPERATURE COATINGS

Kennametal's Hot-Section Materials Development

Russell Yeckley
Kennametal Inc.
1600 Technology Way, P.O. Box 231, Latrobe, PA 15650-0231
Phone: (724) 539-4822, E-mail: Russ.yeckley@kennametal.com

Objective

Determine potential of an existing structural sialon that is being manufactured for other applications that, commensurate with the requirements of advanced microturbines shows potential for strength, environmental stability, and manufacturability for complex shapes.

Highlights

The contract was signed the end of November 2002.

Flexure bars and tile from two sialon compositions have been sent to ORNL for mechanical testing and the Kaiser rig tests.

Technical Progress

Ky1540 is an α-β sialon manufactured for high temperature alloy turning and milling applications. Ky1540's β sialon z value is approximately 0.7. The sialon composite contains 30% α sialon. Sialons located in the region surrounding this composition are being evaluationed for microturbine applications. A screening design of experiments(DoE) will look at the effect of β sialon 'z' value, α content, rare earth level, grain size and grain boundary crystallization on strength, fatigue and oxidation behavior. Mechanical evaluation will begin with two sialons recently sent to ORNL for testing.

Status of Milestones

Delivery of Flexure Bars and Kaiser Rig samples of Sialons selected from screening tests. March 24.

Industry Interactions

Attended the Environmental Barrier Coatings Workshop held in Nashville, TN the first week of November.

Problems Encountered

The sialons are continuous sintered. The hot zone was modified for insert manufacture and the resulting element design causes a temperature gradient. Many of the sialon flexure bars warped

during sintering. Modified loading during continuous sintering or batch sinter will control the warpage. Additional sialon flexure bars and tiles are being fabricated.

Publications/Presentations

'Sialon Material Technology at Kennametal' presentation at the EBC Workshop in Nashville.

Saint-Gobain's Hot Section Materials Development

Robert H. Licht, Vimal K. Pujari, William Collins, Brian LaCourse, Ara Vartabedian
Saint-Gobain Ceramics & Plastics, Inc.
Goddard Road, Northboro, MA 01532
Phone: (508) 351-7815, E-mail: Robert.h.licht@saint-gobain.com

Objective

The goal of this Phase I program is to develop and optimize a high temperature silicon nitride based ceramic material and process suitable for microturbine applications up to 1300°C.

Highlights

The technical effort focused towards optimization of NT154 properties and net shape forming development. NT154 process has been reestablished and flexure strengths approaching 1100 MPa have been achieved. A net shape fully featured integral rotor was successfully formed and densified showing excellent dimensional control.

Technical Progress

The ceramic microturbine technology development effort involved a two-pronged approach as shown in Fig. 1. The material development effort involved the re-establishment of NT154 material, related process and its optimization. Concurrent with

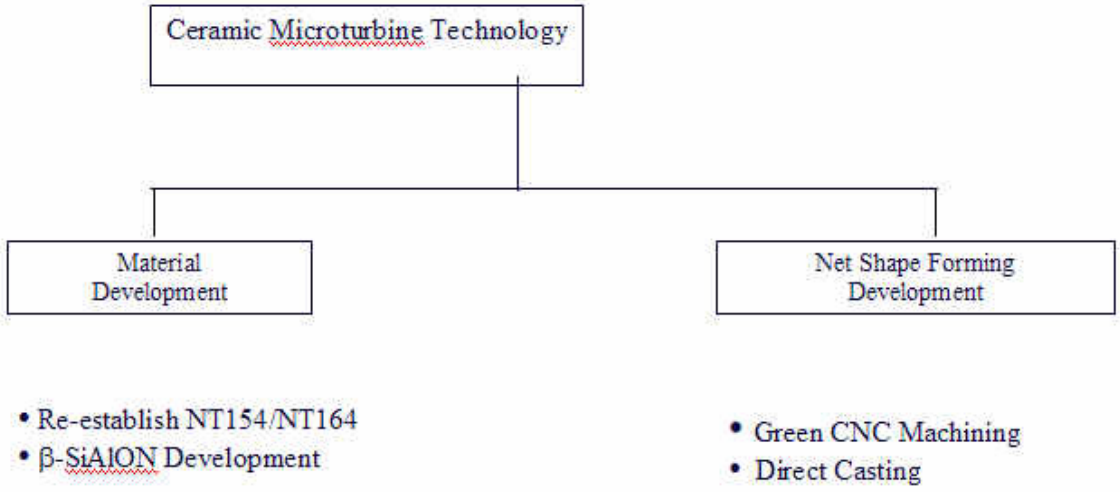

Fig. 1: Ceramic Microturbine Technology

the material development activity, efforts were also directed towards the development of net shape forming technology involving (a) green CNC machining, and (b) Direct Casting. The technical plan for Phase I activity is shown in Fig. 2. The highlight of this approach is (Task 2) to compare mechanical properties derived from standard test tiles and large cross-section specimens simulating net shape formed components.

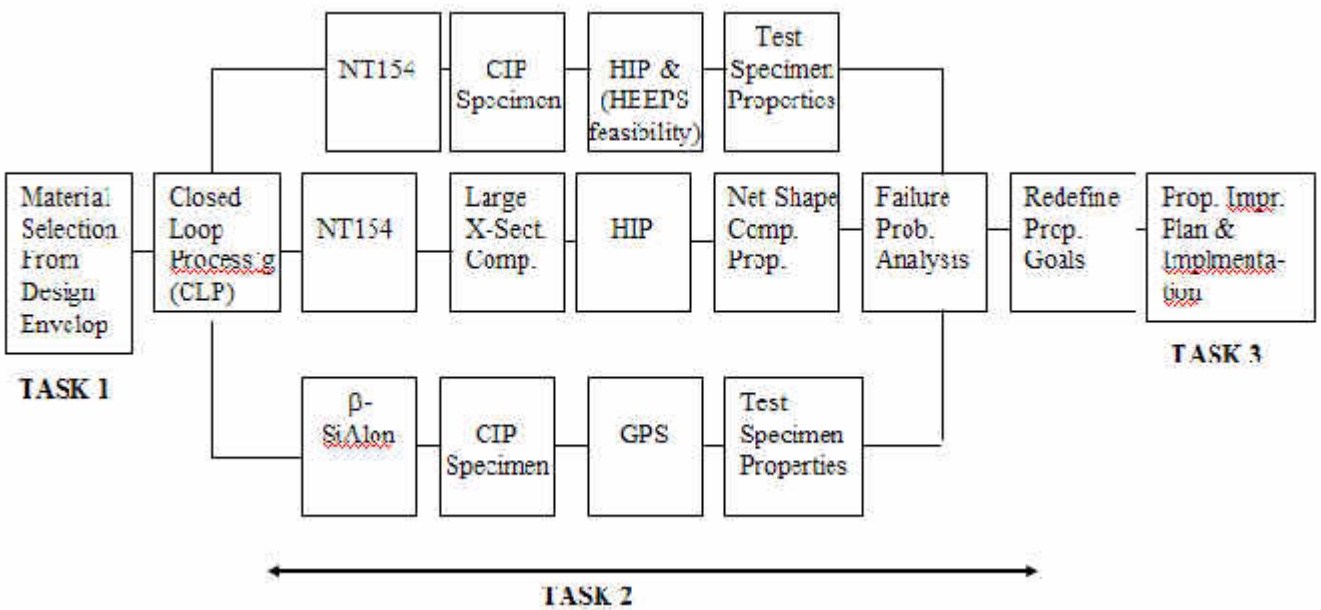

Fig. 2: Hot Section Material Development For Advanced Turbines (Phase I)

1. Material Development

   The development / optimization effort of NT154 silicon nitride composition utilized the well-known concept of processing/microstructure/properties interaction as shown in Fig. 3. Utilizing Closed Loop Processing (CLP) methodology, developed earlier in a Department of Energy funded program, NT154 powder was processed. The process involved milling of silicon nitride powder, along with the sintering aid (yttria) in a Class 10,000 clean room.

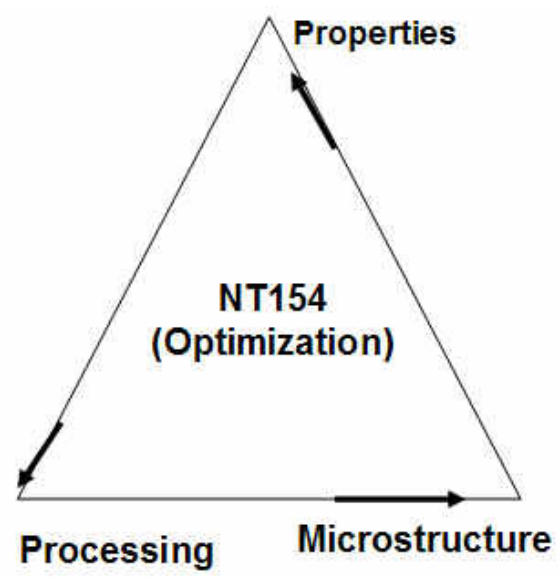

Fig. 3: NT154 Process Optimization

The powder slurry was processed through a mag separator and suitable filters to help eliminate any contaminants. The processed slurry was dried, screened, and subsequently cold isostatically-pressed into test tiles for final densification utilizing glass encapsulated HIP (Hot Isostatic Pressing). In order to achieve full density, along with a suitable microstructure, the HIP process was carefully examined/optimized with the help of a designed matrix of experiments (DoE).

In the HIP DoE, the effects of HIP temperature and hold time were examined. From past studies, suitable ranges of temperature and hold times were assigned to examine their effects on microstructure, density, and α/β ratio and resultant properties such as fracture toughness and room and high temperature 4-point flexure strengths. Based upon this study, a HIP processing condition was subsequently defined to help achieve optimum properties. The predicted optimum condition DoE was experimentally verified as shown in Table 1. Excellent agreement was achieved between predicted and actual HIP process parameters. The optimized NT154 properties from this study are listed in Table 2.

2. Net Shape Forming Development (NSFD)

The NSFD activity involved, as stated earlier, two distinct approaches of Green CNC machining (GCM) and Direct Casting (DC).

2.1 Green CNC Machining (GCM)

GCM effort examined the green (CIP) blank – cutting tool interaction and resultant effects on as-machined surface properties such as roughness parameters (Ra, Rt, Rz), green strength, etc. and tool wear. Based upon this preliminary study, a binder system (GB) and a suitable cutting tool were identified to further optimize the green machining procedure.

With a given binder system and tool type, the green machining procedure was optimized. A designed matrix of experiments (DoE) was laid out utilizing such machining parameters as depth of cut, spindle speed and feed rate. The responses such as machining force and surface finish were optimized. The optimized machining procedure involved the highest material removal rate with minimal pull out and surface roughness.

2.1.1 Machining of Integral Bladed Rotor

A seven bladed axial demonstration rotor (simulating a full scale fully bladed rotor) was machined (Fig. 4a and 4b) utilizing

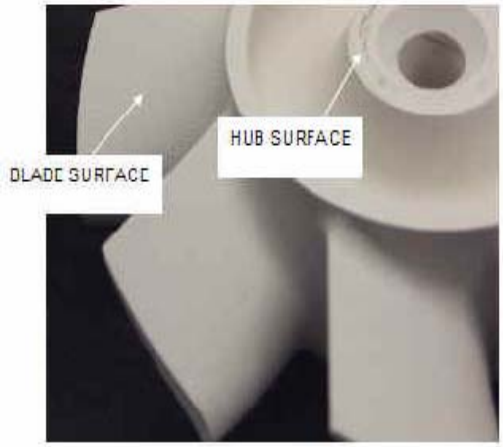

Fig. 4a: Machining of Demonstration Rotors

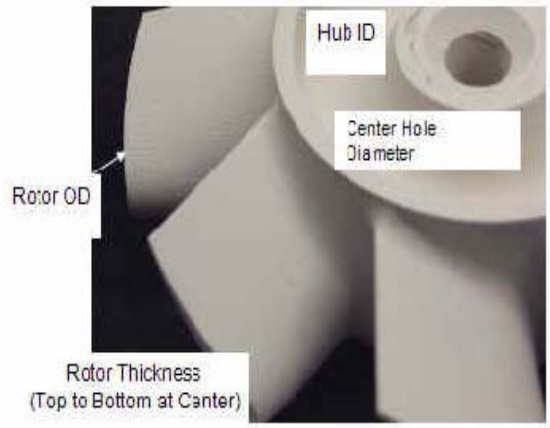

Fig. 4b: Machining of Demonstration Rotors

optimized machining procedure defined above on a 4-axis CNC machine. Two rotors were machined with different feed steps. Small tool feed steps produced blade surfaces with improved surface finish. Table 3 compares the programmed and measured green rotor dimensions. As is obvious, excellent machining dimensional tolerances were achieved.

2.2.2 Densification of Machined Rotor

One of the two green machined rotors was densified using glass encapsulated HIP. A fully densified rotor was measured showing excellent dimensional control. Shrinkage uniformity was measured to be within ±4%. Dimensional control within ±0.003" was achieved. Surface finish of the densified rotor was also measured. After HIP surface, roughness increased by 15%. Further HIP optimization will be targeted to reduce the final Ra from 1.5 μm to 1.0μm.

2.2 Direct Casting (DC) Development

Direct Casting (DC) process entails development of a high solids starch containing slurry and its subsequent casting into a mold as schematically shown in Fig. 5. The key step in the DC process, therefore, is the

Fig. 5: Direct Casting (Starch) of NT154 Complex Shape Components

development of a low viscosity shear thinning slurry with appropriate solids (silicon nitride) loading. The slurry development effort involved identification of a suitable surfactant compatible with the silicon nitride powder as well as the starch particles. Three different slurries so developed and their casting behavior is summarized in Table 4. In this study, the effects of mixing procedures and solids loading were evaluated for their influence on density and surface finish of HIP'ed cast specimens. HIP density approaching 99.1% of T.D. was achieved by enhancing the solids loading in the slurry. In addition, improvements in as-processed (as-HIP surface) surface integrity were also observed in specimens cast with higher solids slurry. Efforts are underway to further improve the quality of cast specimens through improved suspension uniformity and casting procedure.

Status of Milestones

All milestones are on schedule.

Industry Interactions

A meeting was held with UTRC to review the technical progress and ceramic microturbine business plans in November, 2002.

Problems Encountered

None

Publications/Presentations

Attended EBC Workshop in Nashville, TN on November 6-7, 2002 and also reviewed proposed technical plans.

Table 1
Re-Establishing NT154

HIP DoE

	Temperature (C)	Time (min)	Density (g/cm3)	%alpha Si_3N_4	%beta Si_3N_4	Fracture toughness	microstructure
	T1	t2	3.222	28	72	4.50	duplex
	T2	t2	3.223	18	82	4.93	duplex
Prediction	***T2.5***	***t2***	***3.224***	***14.5***	***85.5***	***5.16***	***duplex***
	T3	t2	3.226	0	100	5.23	large grains
	T4	t1	3.225	3	97	5.02	large grains
	T4	t3	3.228	1	99	4.94	large grains

Table 2
Re-Establishing NT154

HIP DoE

		Cerbec SOP 1994	NT154-8 (Netzsch)	NT154-11C (Sweco)	NT154-14A (Sweco)
HIPed Density		**3.22**	**3.22**	**3.22**	**3.225**
Room Temperature Flexure (MPa)	**Min**	**586**	**607**	**662**	**709**
	Mean	**779**	**749**	**948**	**998**
	Weibull	**>8**	**only 8 bars**	**8.6**	**9.7**
High Temperature Flexure (1370C)	**Min**	**455**		**598**	**495**
	Mean	**517**		**604**	**530**
Fracture Toughness	**Mean**	**5**	**4.93**	**5.3**	**5.78***

Table 3
Machining of Demonstration Rotors
Surface Roughness of Green Machined Rotors

Demo Rotor #1 (154-13B-DISK2)	Average Ra (microns)	Average Rt (microns)
Blades Radial	1.25	10.3
Blades Circumferential	2.15	12.5
Top of Hub	0.25	3.6
Bottom of Hub	0.53	6.9

Demo Rotor #2 (154-13B-DISK3)	Average Ra (microns)	Average Rt (microns)
Blades Radial	1.75	10.6
Blades Circumferential	1.09	7.0
Top of Hub	0.22	3.1
Bottom of Hub	0.28	5.2

Dimensions of Green Machined Rotors

All Dimensions in Inches	Green Nominal	Green Actual Demo Rotor #1	Green Actual Demo Rotor #2
Center Hole Diameter	0.380	0.380	0.380
Thickness (Hub Top to Bottom)	1.210	1.211	1.211
OD at Tip of Blades	4.029	4.026	4.024
Outer Hub (near blades) ID	2.034	2.032	2.033
Center Hole Form		0.00017	0.00023
Hub Bottom Surface Form		0.00017	0.00019
Tip of Blades Bolt Circle Form		0.00037	0.00014
ID of Outer Hub (near blades) Form		0.00020	
Offset Between Center Hole and Blade OD	0.000	0.001	0.002
Offset Between Center Hole and ID of Outer Hub	0.000	0.000	0.002

Table 4
Direct Casting of NT154 Specimens

SLURRY	PROCESSING	SOLID LOADING (w%)	VISCOSITY (PaS) @105'	DRYING SHRINKAGE (%)	HIP DENSITY (G/CC)	AS-HIP Surface	MOR (MPa)
5OU Stirred	Silicon Nitride powder added to starch suspension 30 min. deairing	**76.7**	**4**	**2.0± 0.1**	**3.157-3.171**	**Rough**	
5OU Milled	Starch added to milled silicon nitride suspension then stirred 30 min. deairing	**76.6**	**0.3**	**1.8± 0.1**	**3.06-3.09**	**Rough**	
52U Milled	Starch added to milled silicon Nitride suspension, then stirred 30 min. deairing	**78.0**	**0.6**	**1.9± 0.2**	**3.182-3.203**	**Good**	

Environmental Protection Systems for Ceramics in Microturbines and Industrial Gas Turbine Applications
Part A: Conversion Coatings

S. D. Nunn and R. A. Lowden
Metals and Ceramics Division
Oak Ridge National Laboratory
P.O. Box 2008, Oak Ridge, TN 37831-6068
Phone: (865) 576-1668, E-mail: nunnsd@ornl.gov

Objective

Silicon-based monolithic ceramics are candidate hot-section structural materials for microturbines and other combustion systems. The performance of silica-forming ceramic materials in combustion environments is, however, severely limited by rapid environmental attack caused by the combination of high temperature, high pressure, and the presence of water vapor. Thus, the development of environmental protection systems has become essential for enabling the long-term utilization of these materials in advanced combustion applications.

Similar to thermal barrier coatings for nickel-based super alloys, successful environmental protection systems for ceramics and ceramic composites will likely utilize multiple layers, i.e. surface layers and bond coats, and complex combinations of materials. A challenge in the development of current protection systems, most of which employ oxide surface layers, is the formation of silica at the oxide-bond coat or the oxide-substrate interface. The oxide ceramic layers cannot prevent oxygen diffusion to the underlying materials; therefore the formation of silica at this boundary is inevitable.

A solution to the formation of this weak link is the development of substrate compositions or bond coatings that form more thermochemically and thermomechanically stable compounds. A common practice used to improve the performance and extend the life of TBCs for Ni-based super alloys is to enrich the alloy surface with aluminum. The Al surface enrichment using pack cementation or chemical vapor deposition produces a surface layer that forms a stable alumina layer upon oxidation. Similar approaches can be applied to silicon-containing ceramics to produce a bond layer that does not form silica but a more stable oxide. Diffusion processes for surface treatment of silicon-based ceramics will be explored to produce "bond coatings" that will enhance the performance and life of environmental protections systems.

Highlights

Oxidation and corrosion experiments have been started to evaluate the effectiveness of the pack cementation coatings in protecting the silicon nitride substrates. As an initial screening process, thermogravimetric analysis (TGA) is being used to compare the different samples. Using the TGA apparatus, the temperature, heating rate, exposure time, and test atmosphere can be controlled while monitoring the weight change of the sample being tested. This screening test will differentiate between coatings to show compositions that provide beneficial protective

properties. The large matrix of potential coating systems can then be narrowed to focus efforts on the most promising candidates.

Technical Progress

Experiments are continuing to evaluate pack cementation coatings that can be produced on silicon nitride compositions when processed in a nitrogen atmosphere. Samples are being fabricated at temperatures of 1000, 1200, and 1400ºC. The packs contain different reactive elements that interact with the Si_3N_4 surface to form a surface conversion coating. Reactive elements that are being evaluated include: Al, Ca, Cr, Mg, Sr, Y, and Zr. In the pack, these elements are usually added as reactive compounds such as chlorides, carbonates, and nitrates, but may also be in the form of metal powders.

The composition of the Si_3N_4 substrate affects the characteristics of the coating that is formed. This is illustrated in Fig. 1, which shows the differences in the morphology of the coatings that were formed when AS800 and NT154 silicon nitrides underwent an aluminizing pack cementation treatment at 1200ºC in N_2. Although the conversion products that were formed are the same, AlN and Si, the size and distribution of the reactant products is very different, as well as the thickness of the reaction zone. These differences are attributed to the different compositions of the grain boundary phase in the two silicon nitrides.

Figure 2 illustrates the effect of the processing temperature on the resulting pack cementation coating. In this example, NT154 Si_3N_4 was reacted with a powder pack containing $Sr(NO_3)_2$. One sample was processed at 1200ºC, while other was processed at 1400ºC. The composition of the reaction products is still being determined, but the micrographs clearly show the strong differences between the morphology of the coatings and the thickness of the reaction products.

A screening test is being developed to quickly evaluate the oxidation and corrosion resistance of the coated samples. Small segments of Si_3N_4 bars can be tested using thermogravimetric analysis (TGA). In the TGA instrument, the temperature, heating rate, exposure time, and test atmosphere can be controlled while measuring the weight change of the sample being tested. Initial screening tests will be conducted using an atmosphere of water-saturated air at temperatures up to 1350ºC. Baseline data for the uncoated Si_3N_4 materials can be compared to that of the coated samples to identify coatings that provide protection against attack under the test conditions. Promising coatings will be identified for further development and testing.

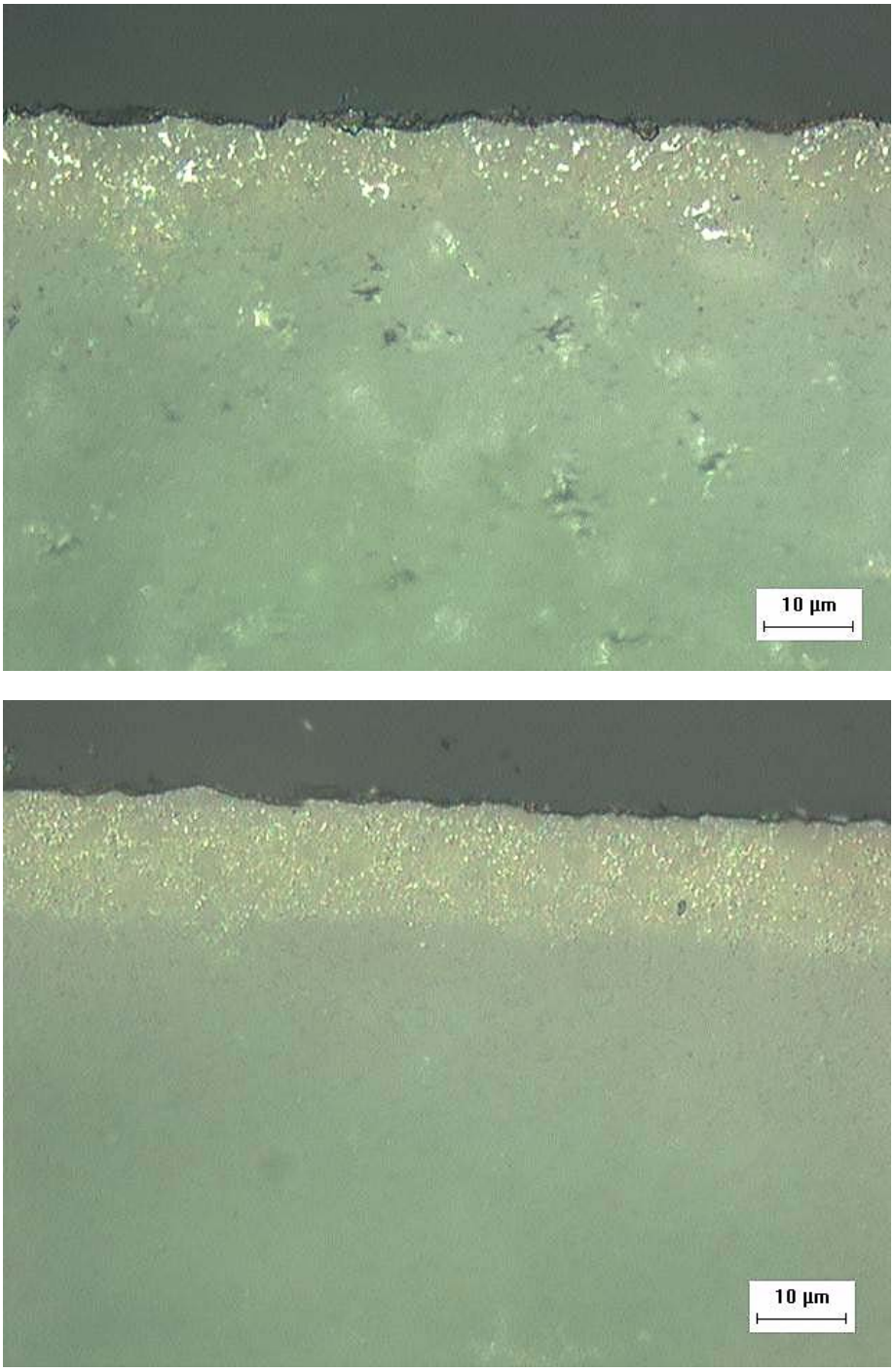

Figure 1. Optical micrographs showing the differences in the morphology of the conversion coatings formed on Si_3N_4 after an aluminizing pack cementation run at 1200ºC. In the top photo, the sample is AS800 Si_3N_4, while in the bottom photo the sample is NT154 Si_3N_4.

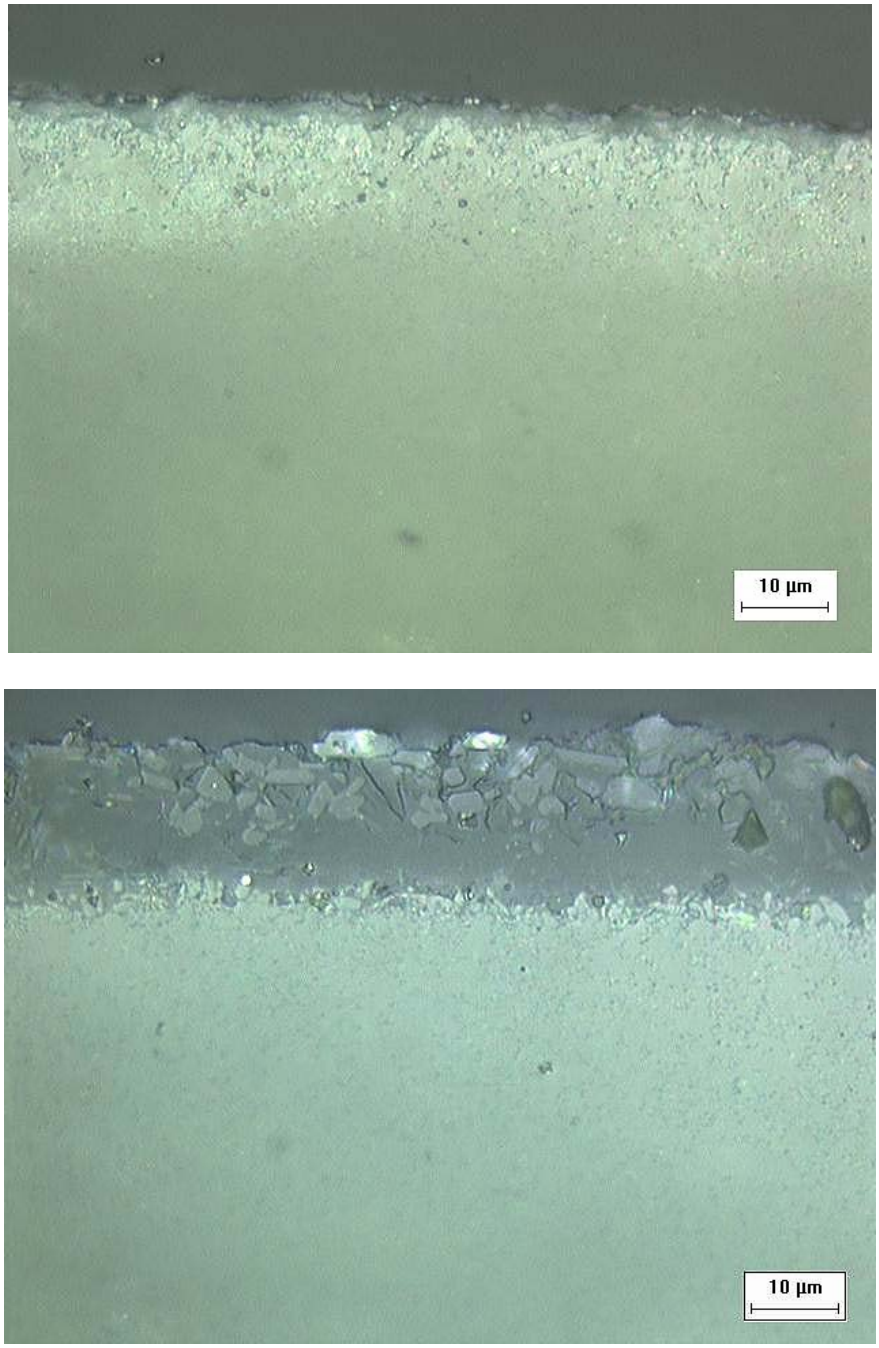

Figure 2. Optical micrographs of NT154 Si_3N_4. The samples underwent pack cementation in a N_2 atmosphere using $Sr(NO_3)_2$ as the reactive component of the pack. The sample in the upper micrograph was treated at 1200ºC, while the sample in the lower micrograph was treated at 1400ºC.

Status of Milestones

Examine diffusion bond coatings containing aluminum for silicon-based ceramics (completed 09/02).

Industry Interactions

None

Problems Encountered

None

Publications and Presentations

A technical presentation entitled “Pack Cementation / Surface Conversion Concepts” was given at the Environmental Barrier Coating Workshop in Nashville, TN on November 7, 2002.

Environmental Protection Systems for Ceramics in Microturbines and Industrial Gas Turbine Applications, Part B: Slurry Coatings and Surface Alloying

B. L. Armstrong, M. P. Brady, K. M. Cooley, J. A. Haynes and H. T. Lin
Metals and Ceramics Division
Oak Ridge National Laboratory
P.O. Box 2008, Oak Ridge, Tennessee 37831-6063
Phone: (865) 241-5862, E-mail: armstrongbl@ornl.gov

Objective

Silicon-based monolithic ceramics are candidate hot-section structural materials for microturbines and other combustion systems. The performance of silica-forming ceramic materials in combustion environments is, however, severely limited by rapid environmental attack caused by the combination of high temperature, high pressure, and the presence of water vapor. Thus, the development of environmental protection systems has become essential for enabling the long-term utilization of these materials in advanced combustion applications.

Similar to thermal barrier coatings for nickel-based super alloys that utilize a specialized oxide surface layer and a metallic bond coat, successful environmental protection systems for ceramics and ceramic composites will likely utilize multiple layers and complex combinations of materials. Most recent efforts have focused on the selection and deposition of the oxide surface layer, and due to numerous factors, the majority of the candidates have been from the aluminosilicate family of oxide ceramics. Stable rare-earth silicate deposits have been found on component surfaces after recent engine and rig tests, indicating there may be other stable oxide compositions that have not been fully investigated. Thin coatings of selected silicate compositions will be deposited on test coupons using a variety of techniques. The specimens will then be exposed to simulated high-pressure combustion environments and materials that demonstrate good potential will be investigated further.

Technical Progress

Work continued on the evaluation of a sacrificial coating or surface alloy to form a volatility barrier. Work also continued on the development of a dip coating process. Characterization of the dispersion of the slurries continued.

Characterization of the BSAS and Mullite Slurries

Measurement of the rheological properties including the effects of aging on viscosity and thixotropy of the BSAS and mullite slurries is on going. The neat (only the binder in solution) binder system chosen for the dip coating was characterized at varying solids loadings under controlled stress and strain experiments. The BSAS and mullite slurries (ceramic suspended in binder solution) are currently being characterized as a function of solids loadings at each binder concentration. Characterization of the zeta potential of the BSAS and mullite powders in aqueous environments was also initiated. The effects of the dispersant, dispersant concentration and aging are currently being examined. The dispersants being used for this study are RT Vanderbilt Darvan C and Rohm & Haas D3021 for the mullite and BSAS systems, respectively,

as based from the sedimentation study completed during the third quarter FY2002. The preliminary results of both the viscosity and surface chemistry analysis show that both the BSAS and mullite slurries would benefit from a different surfactant and potentially a more thixotropic binder system. Pursuit of a new binder system is now on-going.

Norton NT154 substrates were dip coated with mullite or BSAS slurries at varying binder concentrations and heat treated to densify the coating on to the surface of the substrate. An example of a set of the densified mullite coated NT154 samples is shown in Figure 1. As anticipated, as the concentration of binder increased from 1.0 weight % to 2.0 weight % at a constant ceramic solids loading, the final coating thickness increased. As the coating thickness increased, the weaker the coating adherence to the substrate after densification. Edge and corner coating coverage was more complete as the binder concentration increased, however, the coating thickness increased in drying orientation. These results support the preliminary slurry characterization results reported in the previous paragraph. Improvement of either the stability of the existing slurries or the use of a more thixotropic binder system would reduce or eliminate these defects.

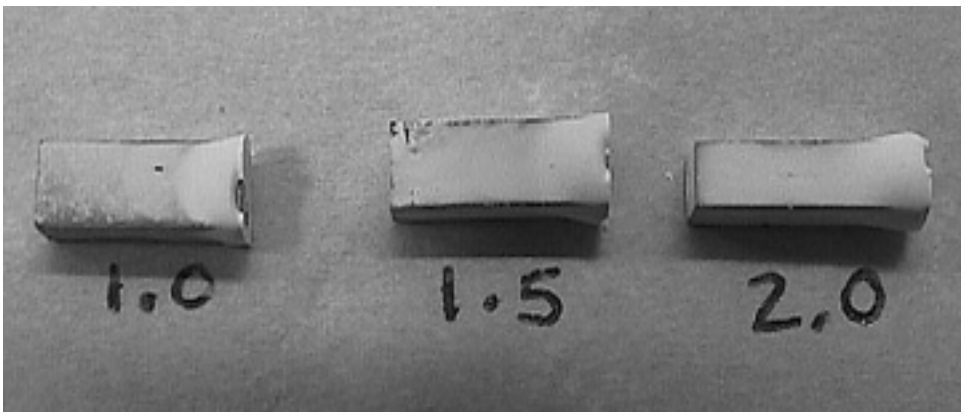

Figure 1. Densified, mullite dip coated Norton NT154 silicon nitride samples. Binder concentration at 1.0, 1.5 and 2.0 weight%.

Development of a Sacrificial Coating

A second approach under exploration is the use of metallic, alumina-forming coatings to protect Si_3N_4. Two concepts are under investigation: 1) a thin metal precursor coating layer that is entirely consumed during a pretreatment to form a mixed and graded alumina based oxide scales and 2) a thick coating of an alumina forming alloy. Alumina was chosen because of its potential to act as a volatility barrier and its relative stability in water vapor. The main drawback is the higher CTE of alumina, which can lead to coating spallation. Initial work has shown that an adherent, self-graded alumina-based oxide layer can be formed on Si_3N_4 by deposition and conversion of thin (1-2 micron) NiAl and TiCrAl precursor compositions. However, some surface cracking of these layers was observed, and further investigation is on going. These findings do, however, demonstrate that thin metallic precursors to form self-graded oxide layers is a viable route to introduce adherent oxide phases on Si_3N_4.

Thicker coating layers, with inner regions that remain metallic, are also being explored because of their ability to provide a continuous source of Al to reform the surface alumina layer. Conventional bond coat compositions based on Fe- or Ni- alumina forming alloys are not

considered viable options because the Fe or Ni base can react with the underlying Si_3N_4 to form low melting point silicide phases. TiCrAl however does not suffer from this limitation, and further TiCrAl alloys have relatively low CTE for a metal, although still considerably higher than Si_3N_4, SiO_2 or alumina. Coupons were sent to M. L. Weaver of the University of Alabama for deposition of 8 - 10 micron thick Ti-51Al-12Cr coatings on Kyocera's SN282 Si_3N_4. These coated coupons were then oxidized in air for three, 100 hr cycles to 1000°C. The alumina scale formed on the TiCrAl coating remained adherent with no evidence of spallation. Surface SEM did, however, reveal the presence of surface cracks in the alumina scale, although the oxidation kinetics for the TiCrAl coated SNS282 were similar to that of a bulk TiCrAl alloy control coupon. RAMAN stress measurements indicated -337±18 MPa compressive stress in the alumina formed on the TiCrAl coated SNS282, compared to a compressive stress of -2893±21 MPa obtained in a similarly exposed bulk alloy coupon of Ti-51Al-12Cr, consistent with surface cracking to relieve the mismatch thermal stress in the coated sample.

Cross-section analysis by SEM and EPMA as seen in Figure 2 indicated a multi-layer structure, consisting of a thin, seemingly protective outer alumina scale overlying a multi-layer structure of Al-rich tau phase (oxidation resistant, Cr-modified Al_3Ti $L1_2$ phase), a Ti-silicide-chromide base phase, and a TiN-base phase (phase identification based solely on EPMA data). There was no evidence of SiO_2 formation or oxygen penetration beyond the outer alumina layer, nor was there evidence of significant Al penetration into the substrate. The observed microstructure suggests the following sequence of events. At the onset of oxidation, Al is selectively oxidized from the TiCrAl to form alumina. At the same time, Ti rapidly back diffuses and reacts with the substrate to form TiN. The back diffusion of Ti is sufficiently more rapid than the selective oxidation of Al that an Al-rich phase (tau phase) is formed underneath the outer alumina layer. The Cr rejected from the oxidation front and Si moving outwards from the substrate also reacts with Ti to form a Ti-silicide-chromide base phase, between the inner TiN base layer and the outer tau layer.

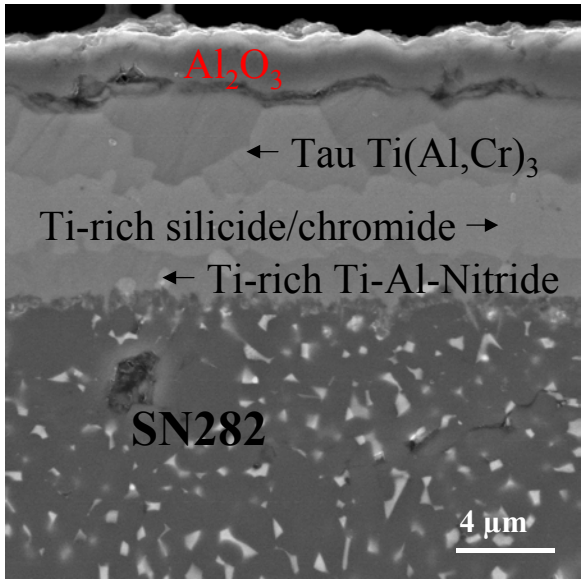

Figure 2. TiCrAl on Kyocera SN282 after exposure to three (3) 100-hour cycles to 1000°C in ambient air

The microstructure resulting from the interaction of TiCrAl and Si_3N_4 under oxidizing conditions supports the concept of a self-graded coating, particularly from the standpoint that an Al-rich metallic layer capable of maintaining alumina-scale formation was formed underneath the alumina scale. The alumina also remained adherent and protective under (light) thermal cycling conditions. However, the surface cracks in the alumina are expected to result in a higher than optimal scale growth rate as the parabolic, diffusion limited growth of a protective scale depends on increased thickness of the scale with time, which is compromised by partial or through cracks. Work in the next quarter will evaluate performance of a similarly TiCrAl coated SN282 in water vapor at 1000°C for three, 100 hr cycles.

Status of Milestones

Evaluate the protective capacity of new silicate coatings on Si_3N_4 in simulated combustion environment. (June 2002)

Evaluate the protective capacity of a slurry coating on silicon nitride in a simulated combustion environment, i.e., the Keiser Rig at ORNL. (September 2003)

Industry Interactions

Discussions with UTRC and GE Corporate R&D have continued. This project has also collaborated with an ARTD Fossil Energy project on Corrosion Resistant Coatings.

Problems Encountered

None

Publications

None

Failure Mechanisms in Coatings

J. P. Singh, Kedar Sharma, and P. S. Shankar
Energy Technology Division
Argonne National Laboratory
Argonne, IL 60439
Phone: (630) 252-5123, E-mail: jpsingh@anl.gov

Objective

The purpose of this proposed research is to identify failure mode(s), understand and evaluate failure mechanisms, and develop appropriate test methods and protocols to characterize the integrity and predict failure of environmental and thermal barrier coatings for advanced turbine applications.

Highlights

Effort during this reporting period concentrated on mechanical evaluation of a set of silicon nitride (AS800) specimens coated with a tantalum oxide (Ta_2O_5) environmental barrier coating (EBC).

Figure 1 (a) shows the cross-sectional micrographs of Ta_2O_5 coated Si_3N_4 (AS800) specimens before and after exposure to simulated service conditions. These micrographs clearly show the Ta_2O_5 top coat and Si_3N_4 substrate. Figure 1 (b) also shows the presence of a crack in the top coat of the exposed coating that extends to the top coat/substrate interface. The formation of cracks in the top coat is believed to result from residual tensile stresses induced by coefficient of thermal expansion (CTE) mismatch between silicon nitride (CTE $\approx 3 \times 10^{-6}$ /K) and the EBC (CTE $\approx 7 \times 10^{-6}$ /K).

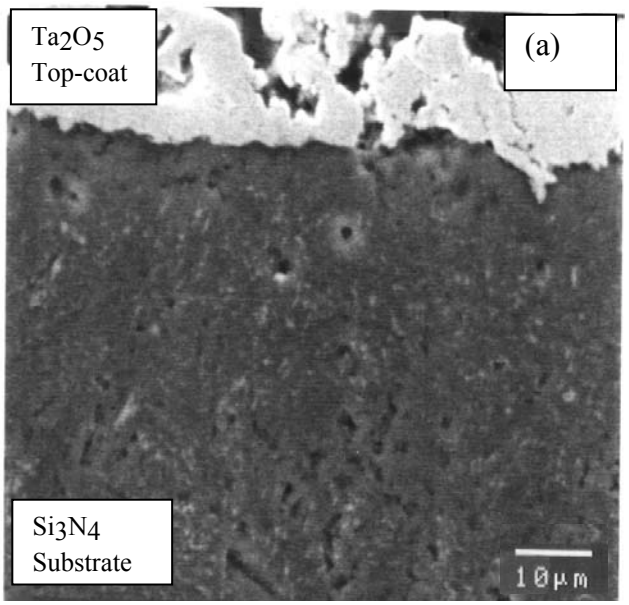

Figure 1 (a). Si_3N_4 in (a) as-coated (AS800-162)

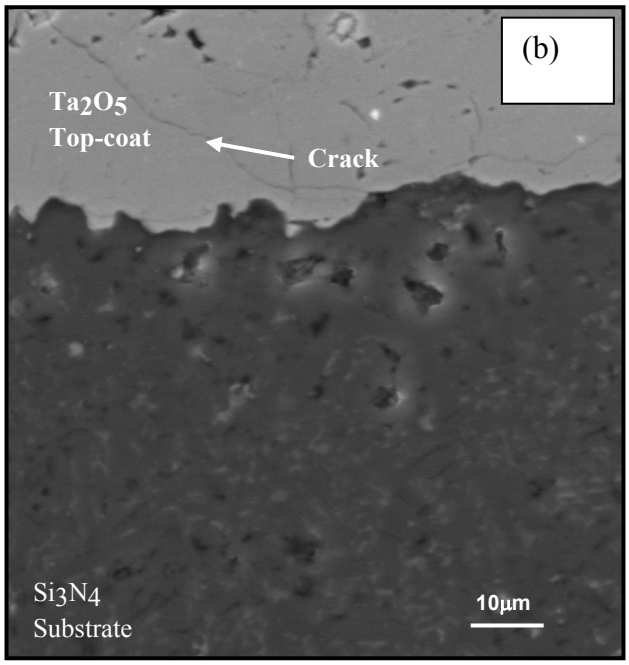

Figure 1 (b). exposed (AS800-129) condition.

Figure 2 shows the fracture toughness variation, measured by indentation technique, as a function of distance from the top coat/Si_3N_4 interface in the as-coated (AS800-162) specimen. The measured toughness shows an anisotropic behavior near the interface. In the interfacial region, the toughness (≈2 MPa√m) in the direction parallel to the interface is lower than the toughness (≈ 9.5Mpa√m) in the normal direction. It was observed that in the bulk region (away from the interface), indentation cracks in both perpendicular and parallel to the interface were approximately of the same size. The average toughness of the bulk was calculated using an average value of the crack lengths in both parallel and perpendicular directions. In contrast, near the interface, the indentation cracks in a direction perpendicular to the interface were much shorter than the cracks in the parallel direction. Therefore, fracture toughness values (upto ≈**2**00 μm from the interface) were calculated by measuring the crack lengths either in parallel or in perpendicular direction, as shown in the figure. The toughness behavior of the exposed specimens followed a similar pattern as observed in the as-coated specimen. This anisotropy in toughness is believed to be due to the presence of anisotropy in residual stress distribution at the interface.

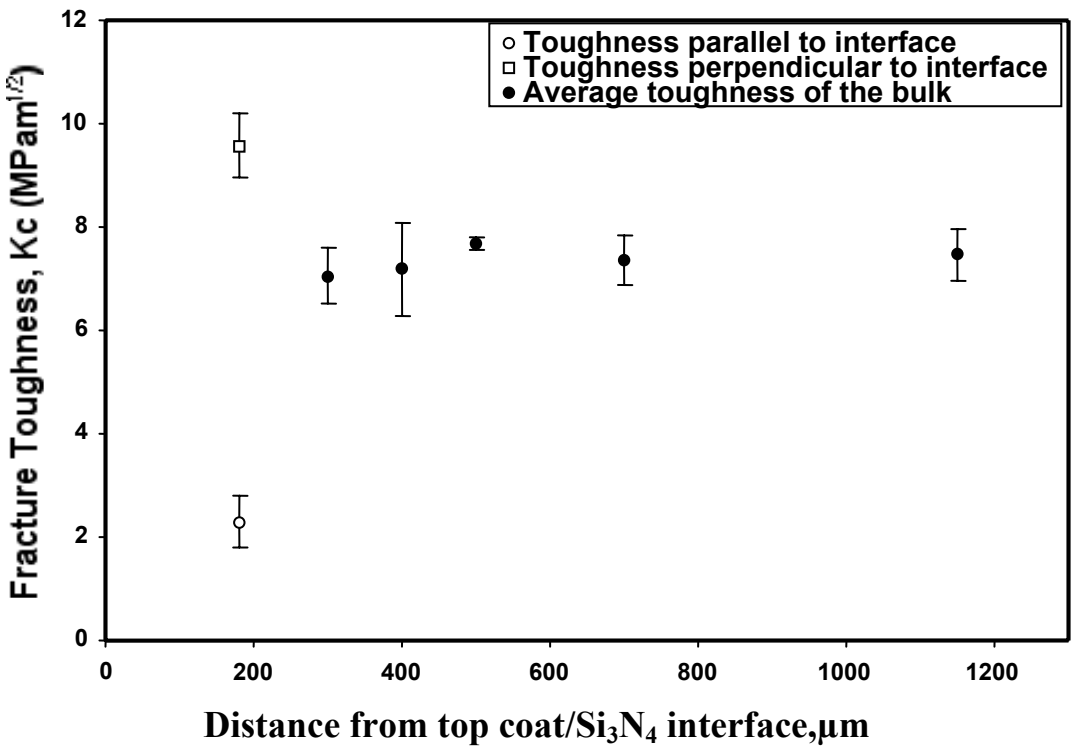

Figure 2. Measured values of fracture toughness at increasing distance from the top coat/Si_3N_4 interface for as-coated Si_3N_4 (AS800-162) specimen. Open symbols represent the fracture toughness values calculated by measuring the crack lengths either parallel or perpendicular to the interface, while close symbols represent average fracture toughness of the bulk, calculated based on the average crack lengths measured both in parallel and perpendicular directions to the interface.

Status of Milestones

Complete mechanical evaluations of a set of EBC specimens and initiate correlations of the mechanical property data with microstructural changes in EBCs during exposure to simulated service environments. February 2003.

Presentations

J. P. Singh presented a keynote talk entitled "Damage Evolution and Residual Stress Measurements in Ceramic Coatings" at the Asian International Symposium on the Science of Engineering Ceramics, November 4-6, 2002, Osaka, Japan.

High-Temperature Diffusion Barriers for Ni-Base Superalloys

B. A. Pint, K. Cooley and J. A. Haynes
Metals and Ceramics Division
Oak Ridge National Laboratory
Oak Ridge, TN 37831-6156
Phone: (865) 576-2897, E-mail: pintba@ornl.gov

Objective

Nickel-base superalloys require coatings to improve their high temperature oxidation resistance, particularly when a thermal barrier coating is employed. The underlying oxidation-resistant metallic coating or bond coat is degraded by the loss of Al due to oxidation but much more Al is lost due to interdiffusion with the superalloy. Loss of Al causes diffusion aluminide coatings to undergo phase transformations which likely cause deformation of the bond coat surface and subsequent loss of the protective alumina scale and the overlying thermal protection layer. The goal of this program is to fabricate and assess potential compounds for use as high-temperature diffusion barriers between coating and substrate. Ideally, the barrier would act to reduce the inward diffusion of Al as well as the outward diffusion of substrate elements (such as Cr, Re, Ta, W) which generally degrade the oxidation resistance of the coating. The work is motivated by previous experimental results which suggested some compositions that exhibited diffusion-barrier capabilities. A secondary objective is to demonstrate routes to fabricating diffusion aluminide coatings incorporating a diffusion barrier using chemical vapor deposition (CVD).

Highlights

Characterization of aluminide coatings with a Ni-Hf barrier layer was conducted in the as-deposited condition and after various increments of cyclic oxidation testing at 1150°C and the results compared with coatings without a barrier layer. After exposures at 1150°C, the coating with a barrier layer showed a slight reduction in the amount of β-NiAl phase depletion but otherwise there was no significant difference in the coating composition. Different barrier layer compositions and lower temperatures are now being investigated.

Technical Progress

<u>Coating Fabrication</u>
Fabrication of CVD NiAl coatings over various thicknesses of sputtered Hf candidate diffusion barrier layers continued this quarter. The coatings were made using a laboratory-scale CVD reactor at 1100°C, as described in previous reports. Throughout this report Hf thickness refers to the thickness of Hf deposited on one face of the superalloy substrate by sputter coating prior to aluminizing. Some Hf is lost due to chlorination during the aluminizing process. The resulting coatings on the Hf-coated surfaces had complex microstructures that were characterized using electron microprobe analysis (EPMA). The coatings consisted of several layers, as shown in Figure 1. These layers include: (1) a surface layer of single-phase β-NiAl (up to 25 μm thick), (2) a thinner Ni-Al layer with Hf-rich precipitates, (3) a porous layer of Ni-Al with smaller precipitates, (4) a Ni-Hf layer with some incorporated Ta-rich particles, and (5) the typical interdiffusion zone that results from aluminizing a Ni-base superalloy (General Electric Aircraft Engine's René N5) via low activity CVD processing. To better visualize the elemental distribution of the as-deposited coating, various elemental maps from the highlighted area in Figure 1 are shown in Figure 2. A CVD coating without the Hf sputter layer would consist of only the NiAl layer and the interdiffusion zone. As can be seen

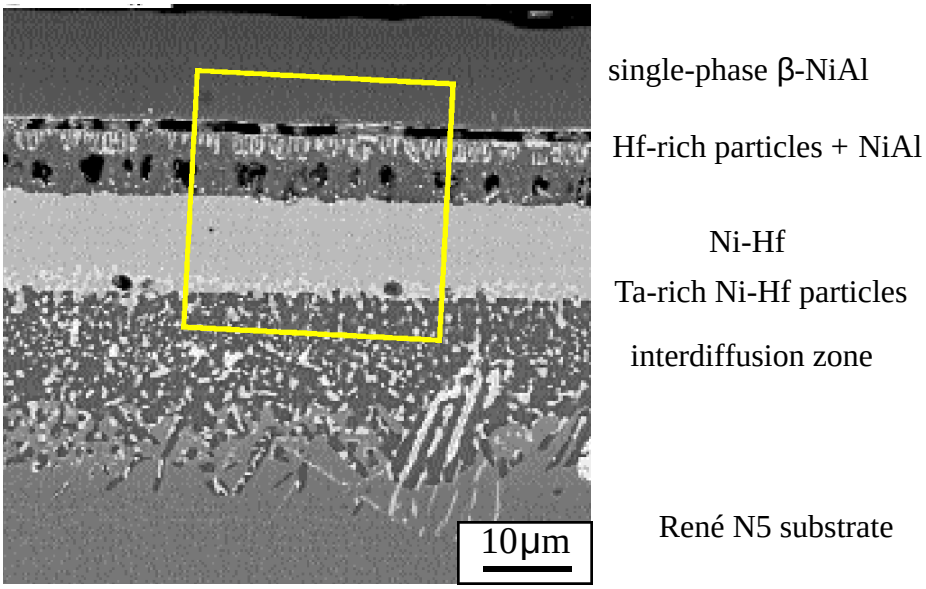

Figure 1. Secondary electron image of a metallographic cross-section of the Hf-containing surface of an as-deposited CVD NiAl coating (6h, 1100°C) fabricated from a specimen with a 7 μm thick layer of sputtered Hf on one surface.

from Figure 1, it was common for cracking to be present between the NiAl layer and the underlying coating. This cracking led to early failures in oxidation testing as noted in the previous report.

As-coated specimens with a 4μm Hf layer were examined after 2h and 6h (H4.10 and H4.4, respectively in Table I) of aluminizing at 1100°C to examine the development of the layered structure. Figure 3 shows back-scattered electron images of the two stages. Another difference between the two specimens is that H4.4 received a 10min anneal at 700°C in the reactor prior to aluminizing while H4.10 received a 1h, 800°C anneal. This difference may have affected the development of the Ni-Hf layer which is more prominent with the shorter anneal but longer aluminizing time of H4.4, Figure 3b. Line scans using EPMA showed that H4.4 contained significantly more Hf than the H4.10 which was aluminized for a shorter time, Figure 4a. Thus, the anneal prior to aluminizing appears to have further removed Hf from the substrate or hastened its evaporation after aluminizing began. The line scans also showed that the aluminide layers on either side of the specimen (with and without the Hf layer) were of similar thickness and Al concentration, Figure 4b. For example, after 2h, the aluminide layer was 21.6μm thick on the Hf-coated side and 22.4μm thick on the Hf-free side. Near the specimen surface, the Al content on the Hf-coated side was 6% higher, Figure 4b, but dropped to comparable levels within a few microns. After 6h, the total coating thickness on the Hf-free side was

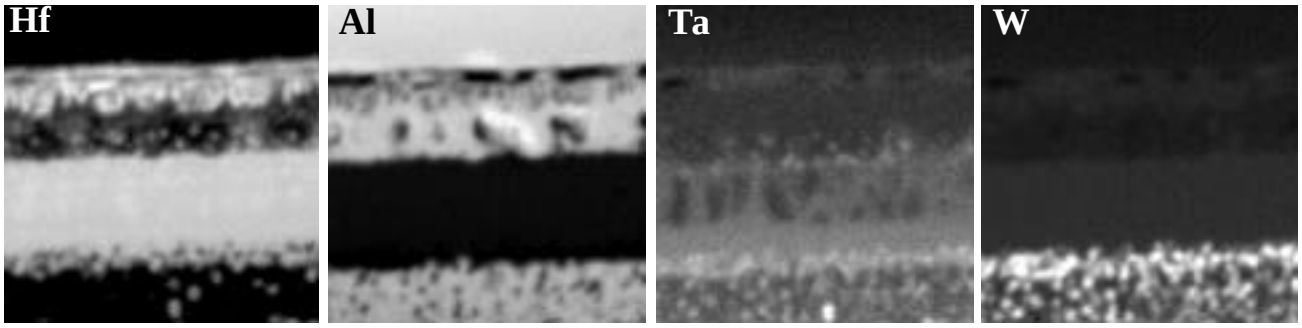

Figure 2. EPMA elemental maps of Hf, Al, Ta and W from the marked region in Figure 1.

Table I. Fabrication of CVD aluminide coatings with and without sputtered diffusion barriers

Specimen	Hf Thickness* (µm)	Pre-Aluminizing Heat Treat	Time (h)	Mass Gain (mg)
N5-1	uncoated	700°C, 10min	6	20.9
N5-2	uncoated	700°C, 10min	6	20.3
H4-4 (as-coated)	4	700°C, 10min	6	13.4
H4-5 (100h, 1150°C)	4	800C, 10 min	6	19.9
H4-6 (200h, 1150°C)	4	700°C, 10min, 800°C 20min	6	10.6
H4-10 (as-coated)	4	800C, 1h	2	0.3

* Specimens were sputter coated on one side prior to aluminizing.

slightly thicker (44µm) than the Hf-coated side (42µm). As after 2h, the near-surface region of the Hf-coated side had a higher Al content but otherwise the profiles were similar. The most striking difference on the Hf-coated side was the intermediate Ni-Hf layer which contained only 5% Al, arrow in Figure 4b. This layer was not distinctly observed on the specimen aluminized for only 2h.

Characterization of Specimens After Oxidation Testing

As-deposited CVD NiAl coatings with various Hf-based barrier layers beneath the coating were exposed to cyclic testing at 1150°C in dry, flowing O_2. Cycles consisted of 60 minutes at temperature and 10 min cooling to ambient temperature. Specimen mass changes and scale morphologies were reported previously. Specimens with 7µm Hf layers tended to fail rapidly during cyclic oxidation testing, due to the development of porosity within the Hf-rich layer and subsequent buckling and cracking of the NiAl coating. Hafnium chlorination/volatilization during CVD aluminizing resulted in a very low Hf content for the 1µm sputter coatings. Due to these difficulties with the 1 and 7µm coatings, the characterization work focused on coatings with 4µm Hf layers.

Specimens H4.5 and H4.6 (Table I) were exposed for 100 and 200 1h cycles at 1150°C, respectively. Cross-sections of the Hf-coated and uncoated sides of each specimen are shown in Figure 5. If the Ni-Hf diffusion barrier were effective in reducing the loss of Al to the substrate, the remaining coating should be thicker or contain a higher Al content than the opposite side of the specimen which does

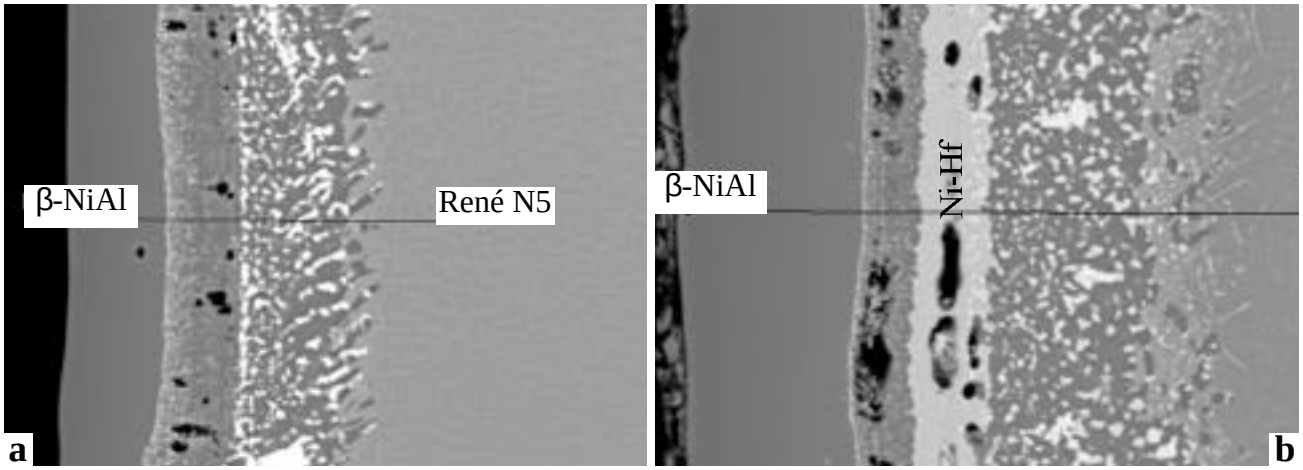

Figure 3. SEM back-scattered electron images of polished cross-sections of the coatings formed after (a) 2h (H4.10) and (b) 6h (H4.4) of aluminizing at 1100°C.

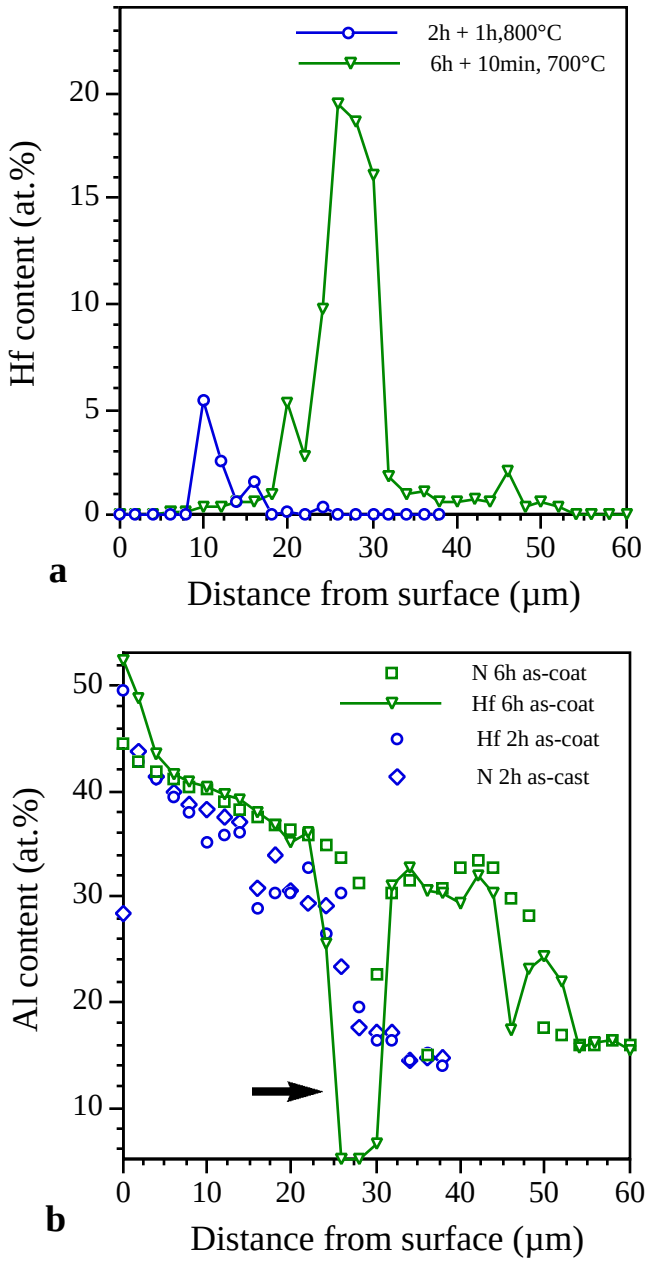

Figure 4. Line scans from the coating surface of the as-deposited coatings H4.10 (2h) and H4.10 (6h) showing the (a) Hf contents and (b) Al contents. The Hf and N notations in (b) mark the Hf-coated and uncoated sides, respectively.

not have a Hf-rich coating. However, the aluminide layer on each side of these specimens was similar in thickness after each exposure. Figure 6 shows the EPMA line profiles of the Al content in each of the cross-sections shown in Figure 5. In the locations where the line scans were conducted, the Al contents are indistinguishable on the Hf-coated and uncoated sides of the specimens. Unlike the as-coated Al profile, after exposure at 1150°C the Al content was uniform in the outer aluminide layer. The average Al content in this layer dropped very slightly between 100 and 200h. The thicker layer observed after 100h is partially due to a thicker starting coating reflected in the higher mass gain for this specimen, compare specimens H4.5 and H4.6 in Table I.

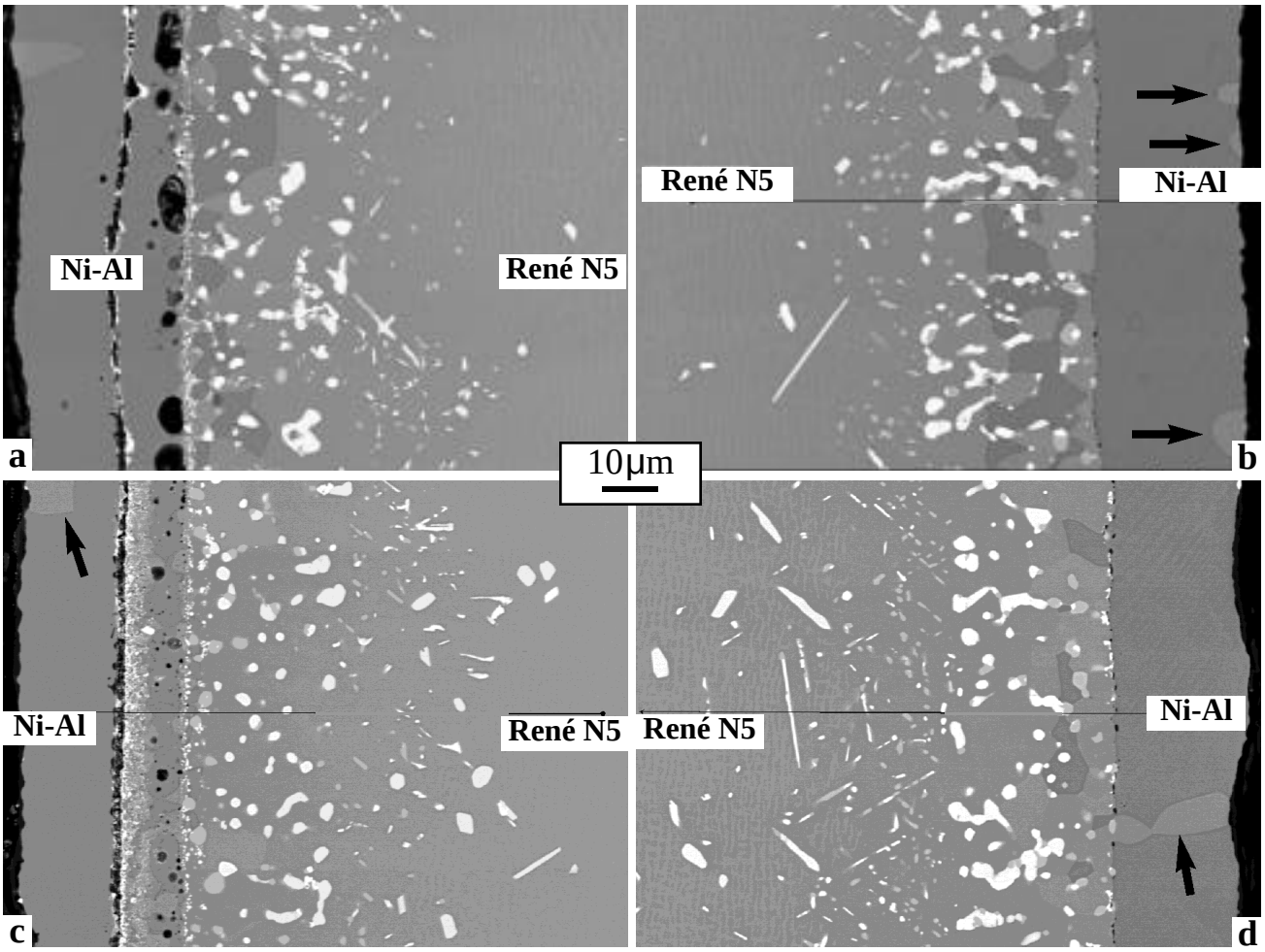

Figure 5. SEM back-scattered electron images of polished cross-sections of the coatings after exposure for (a,b) 100h at 1150°C and (c,d) 200h at 1150°C. (a) and (c) show the Hf-coated sides and (b) and (d) show the uncoated sides.

For both of the specimens, there was one notable difference between the Hf-coated and uncoated sides. The Hf-free coatings contained more low-Al regions in the outer aluminide coating than the Hf-coated side. These regions are brighter in the back-scattered images and are marked by arrows in Figure 5. One region is clearly seen in the Al map in Figure 7. The number and size of these regions increased after the 200h exposure as expected. While this may indicate some benefit of the Ni-Hf layer as a diffusion barrier, it was limited at best. Additional testing will be conducted to determine if the benefit is greater at lower exposure temperatures.

The next phase of this study has been initiated to look at Engel-Brewer compounds as diffusion barriers. Using what has been learned in the first phase of this study, the first attempt will be to form a $HfPt_3$ layer using sputter deposits of various thicknesses of Hf and Pt.

Status of Milestones

FY2003
Complete testing and characterization of Hf-containing diffusion barriers including a performance comparison with state of the art bond coatings and report experimental results in draft report for

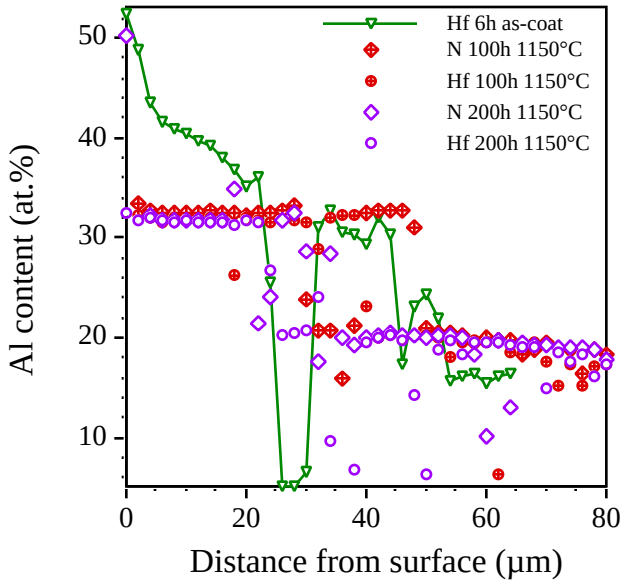

Figure 6. EPMA line scans of the Al content from the coating surface of the specimens exposed for 100h and 200h at 1150°C compared to the as-deposited coating. The Hf and N notations indicate the Hf-coated and uncoated sides, respectively.

publication. (August 2003)

Industry Interactions

The project team had interactions with Pratt & Whitney in East Hartford, CT about a possible collaboration.

Problems Encountered

None

Publications

None

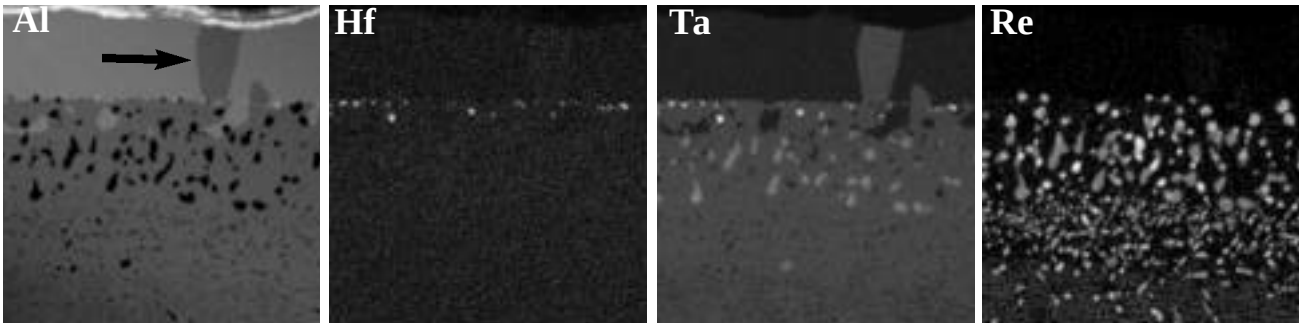

Figure 7. EPMA elemental maps of Al, Hf, Ta and Re from the Hf-free side of H4.6, exposed for 200, 1h cycles at 1150°C. The Al map shows a bright layer at the surface due to the Al_2O_3 scale. The Al-depleted phase (arrow) also was rich in Ta.

POWER ELECTRONICS

Development of High-Efficiency Carbon Foam Heat Sinks for Microturbine Power Electronics

R. D. Ott, B. L. Armstrong, J. W. Klett
Metals and Ceramics Division
Oak Ridge National Laboratory
P.O. Box 2008, Oak Ridge, TN 37831-6083
Phone: (865) 574-5172, E-mail: ottr@ornl.gov

Objective

There are situations in hot climates or enclosed spaces where it is very difficult to sufficiently cool the power electronics of today's microturbines utilizing conventional heat sinks. In order for these heat sinks to adequately control the heat loads of advanced high-efficiency microturbines they must be rather large and heavy. Therefore, ultra-efficient heat sinks that utilize lightweight, high conductivity, high surface area graphite foam are being developed.

Highlights

Graphitic foam was densified with naphthalene which was subsequently converted to graphitic carbon to form a foam reinforced carbon-carbon composite using a novel process developed by the U.S. Air Force and licensed to SMJ Carbon. The densification was performed to produce dense foam-reinforced materials of which mechanical and thermal properties could be measured. It was found that after 6 densification cycles, thermal conductivity increased by 80 W/(m·K) in the z-direction and 50 W/(m·K) in the x-y plane and was relatively independent of the original properties of the foam. The compressive strength also increased by a factor of 4 and was again relatively independent of initial compressive properties of the foam.

Technical Progress

Graphitic foams with bulk thermal conductivities up to 180 W/(m·K) [1] have been demonstrated to be good heat transfer mediums. The combination of an open cellular structure and a thermal conductivity to weight ratio (κ/ρ) of greater than 200 (compared to 45 for copper) for this material presents an opportunity to radically change the solutions to many heat transfer problems. The unique graphitic foam has been evaluated for incorporation as the core of heat transfer devices, such as radiators and heat sinks, as well as in evaporative cooling and phase change energy absorption devices. However, in many instances the low density and low strength limits its applicability. For example, machining a radiator with small fins out of the foam can be misleading. While it has a higher surface heat transfer coefficient [2], the fins can only be around 2 mm thick due to mechanical stability, compared to less than 0.5 mm for aluminum fins.

Thus, even though the graphitic foam heat exchangers have been shown to have higher power densities, the fins in the foam radiator have to be packed so tightly that the pressure drops through the radiator increase to a point where it no better than an aluminum finned radiator. Therefore, densification methods similar to those used to make carbon-carbon composites are attractive to increase not only the density and strength of the foam, but the thermal conductivity

as well. A novel low-cost densification process developed at the US Air Force Research Lab Propulsion Directorate, Edwards AFB, CA and licensed to SMJ Carbon Technology [3] has successfully been used to densify a carbon fiber preform to between 45 and 80% solid in less then two weeks (depending on number of densification cycles). This densification process has the potential to produce thermally conductive structural graphitic foam with a wide range of applications from traditional thermal management devices to friction and wear articles.

The SMJ Carbon densification process is relatively simple. First, a hydrocarbon feedstock, such as naphthalene, is impregnated into a porous carbon product, such as a carbon fiber preform or carbon foam. Then under pressure and with temperature, the naphthalene is converted to mesophase pitch, which at higher temperatures is eventually converted to a graphitic structure. The cycle time can be less than 24 hours and the pressures during impregnation are relatively low because of the low viscosity of the naphthalene. Compare this cycle with the conventional pitch densification processes which can take many days at extremely high pressures, > 340 Mpa (50,000 psi). A complete densification with numerous cycles using the SMJ Carbon method may be completed in the time it takes for one densification cycle using conventional techniques. This process should be well suited for densification of the graphitic foams to increase both the mechanical and thermal properties.

To examine the effects of the SMJ process on the graphitic foam, several billets of foam were produced "in house" using different processing conditions. Billets 180 and 185 were graphitized at 1°C/min to 2800°C and then cut in half. One half of each billet was retained as a control while the other half was densified with 6 cycles of the SMJ Carbon process and then graphitized again at 10°C/min to 2800°C. The control samples and the densified samples were machined into specimens and tested for the compression strength and thermal conductivity according to ASTM C714 and C695, respectively.

The results of the first set of tests illustrate the effects of densification on the density, compression strength and thermal conductivity of the first billets of foam (Table I). The progressive weight change for the entire billet with each densification cycle is shown in Figure 1. Initial weight gain was rapid, but as the pore size decreased with densification, the efficiency of the subsequent infiltrations decreased significantly (Figure 2). The density of the billet increased from 0.49 to 1.07 g/cm^3 with six cycles and less than one week of processing time. The less dense more open structure of sample 180 allowed for higher weight gain. Scanning electron microscope images of the "raw" foam and the densified foam show that the material added during densification appears to uniformly coat the surfaces of the foam and increase the ligament thicknesses (Figures 3 and 4).

Sample 180 had significantly lower thermal conductivities in the foaming direction (z-direction) for both the raw and densified state as compared to sample 185. However, for both samples, the addition of the highly graphitic matrix material produced an increase of roughly 70 - 80 W/(m·K) in the thermal conductivity in the z-direction, and nearly 50 W/(m·K) in the x- and y-directions. The densification increased the thermal conductivity at a consistent rate, independent of the starting thermal properties of the foams. As seen in Figure 5, the densification appeared to simply shift the thermal conductivity profiles, indicating that the initial foam thermal conductivity was the predominant factor in the final products thermal conductivity.

As shown in Figure 6, the compression yield strengths of the raw foam were essentially independent of the foaming conditions. The strengths of the densified foams were on average four times that of the raw foam while the densities more than doubled. This indicates that the densification process is likely filling or healing microcracks within the original foam, increasing the strength of the base foam. The stress-strain behavior for the densified foam is similar to that of the raw foam (Figure 7) in that an initial peak stress is reached then the stress oscillates with further strain. However, the stresses in the densified foam reduce with continued strain, possibly indicating crack propagation through the material.

Table I. Comparison of ORNL graphite foams before and after 6 densification cycles.

Sample ID	# of densification cycles	Euclidian Density, ρ	Relative Density	Thermal Conductivity				Comp. Yield Strength
				X	Y	Z	Z/ρ	
		g/cm^3	%	W/mK	W/mK	W/mK	$\frac{W/mK}{g/cm^3}$	MPa
180 A	0	0.49	20	43.3	38.0	106.3	231	1.7
180 B	6	1.07	48	97.2	92.9	186.7	179	7.2
185 A	0	0.54	21	54.1	56.5	157.2	326	2.1
185 B	6	1.03	46	94.4	93.7	221.1	215	8.5

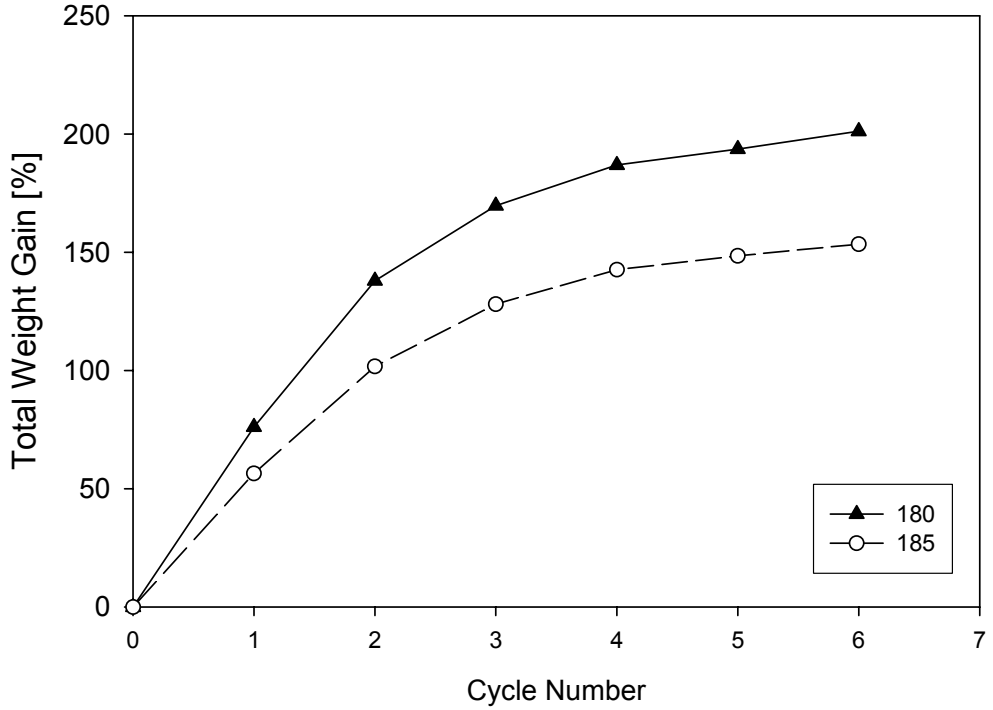

Figure 1. Progressive weight change of entire billet with densification cycles.

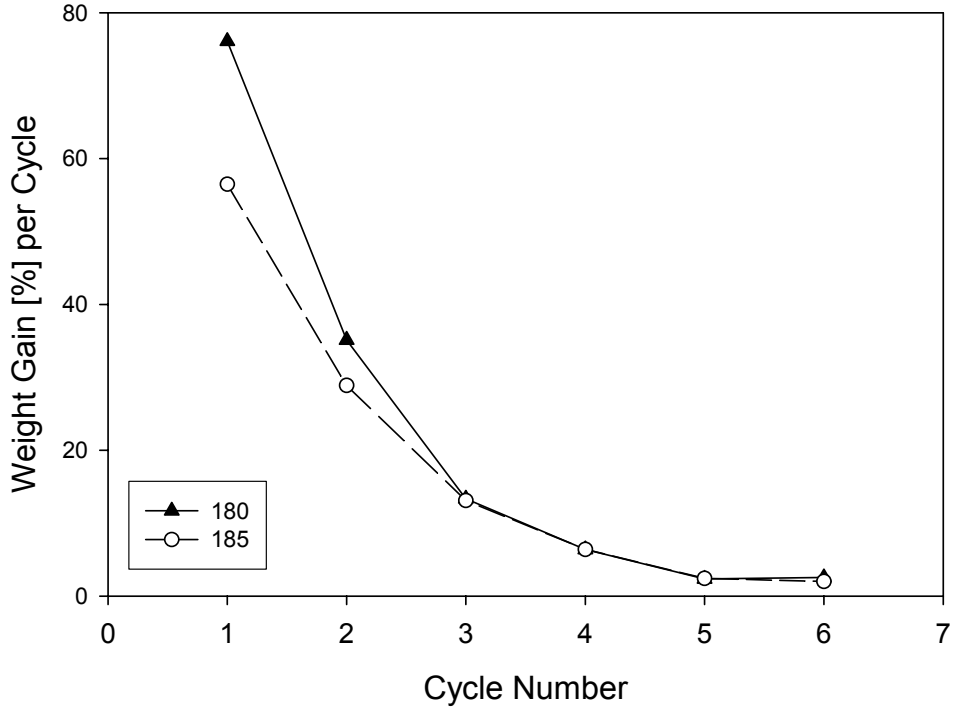

Figure 2. Progressive impregnation efficiency as a function of number of densification cycles.

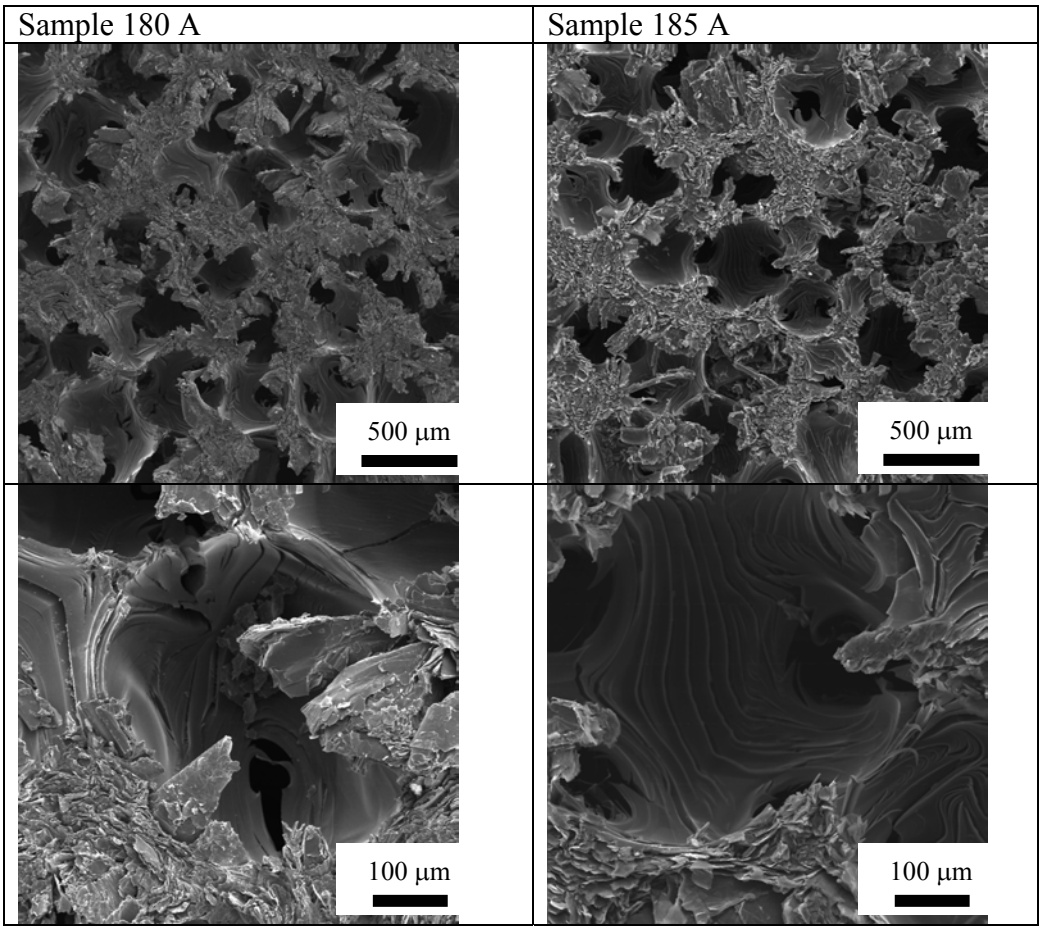

Figure 3. Typical SEM images of the raw foams.

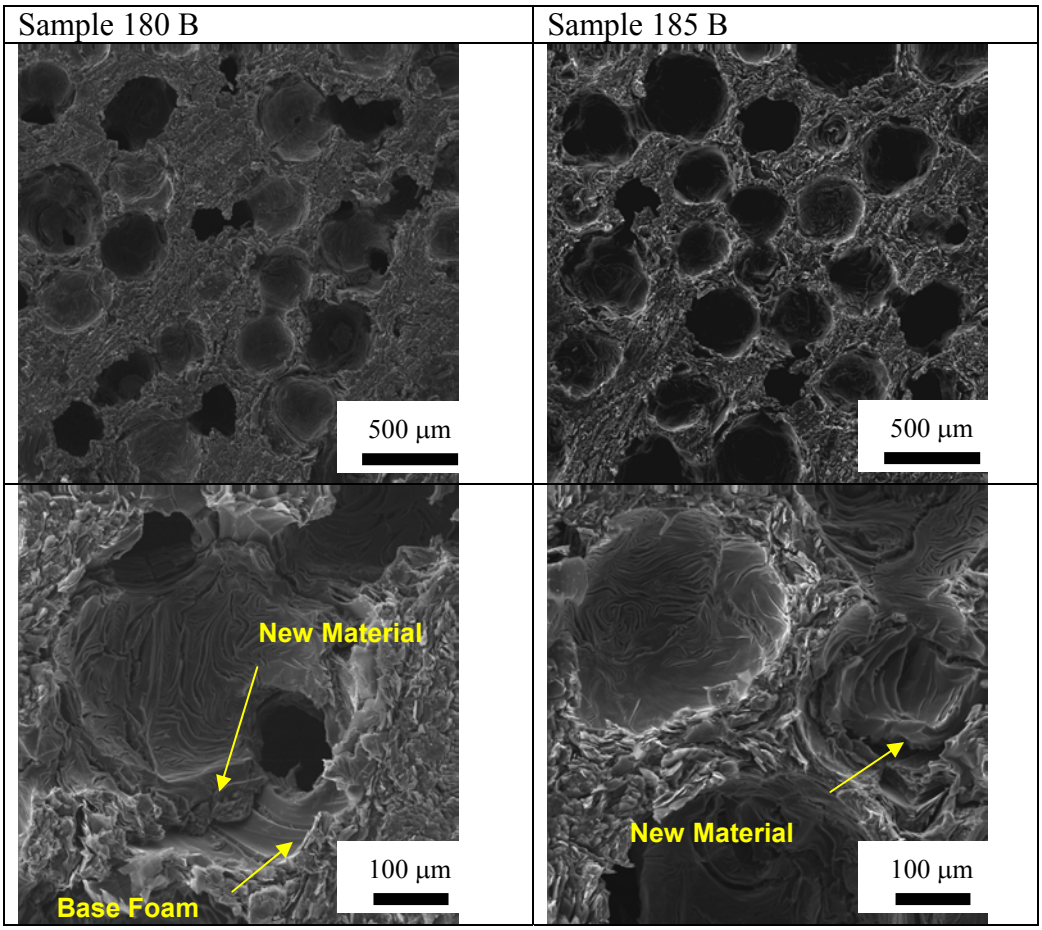

Figure 4. Typical SEM images of the densified foams.

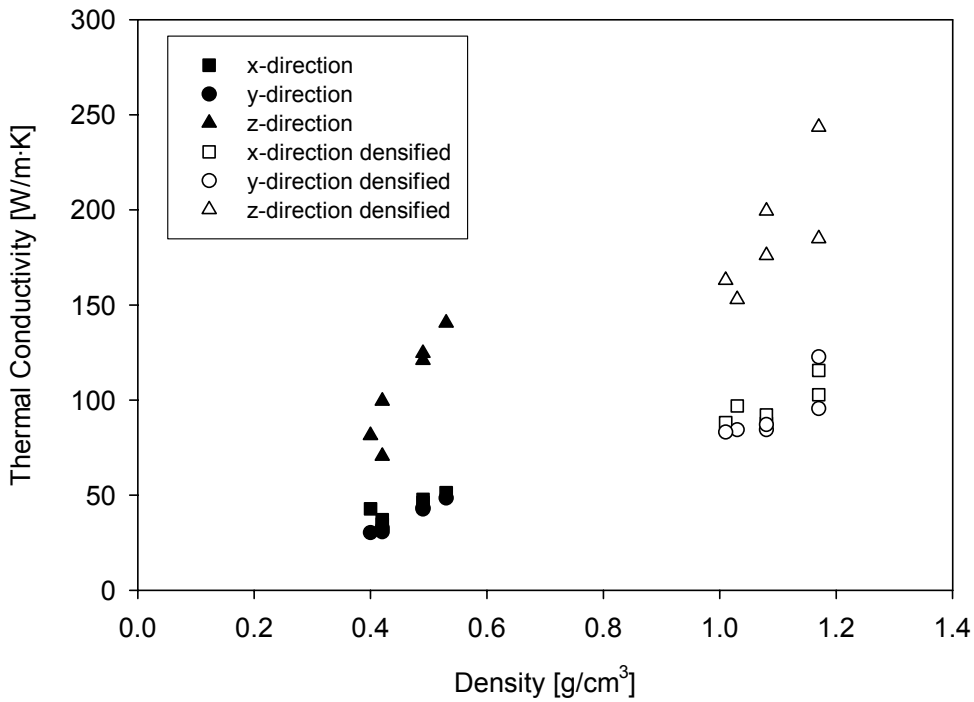

Figure 5. Thermal conductivity of samples from billet 180 before and after densification with SMJ process.

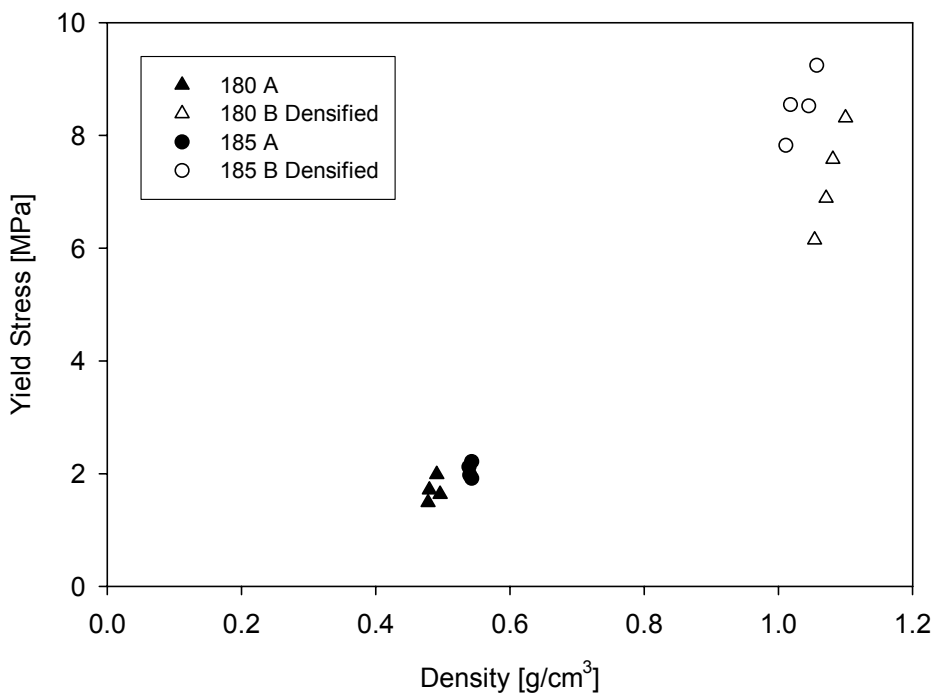

Figure 6. Compressive yield stress of the raw and graphitized foams.

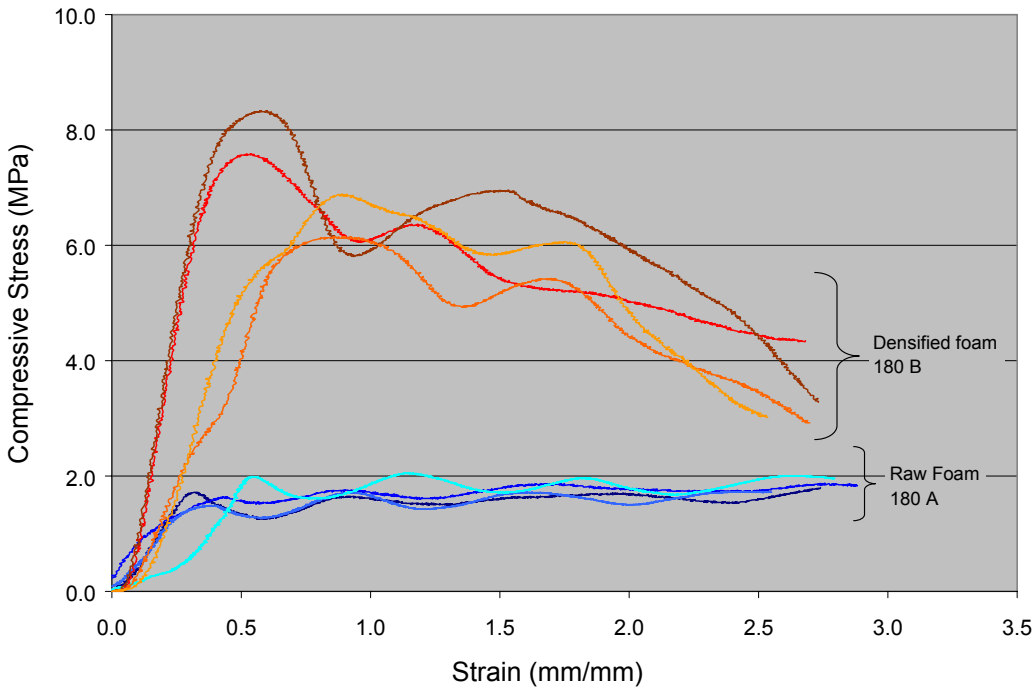

Figure 7. Typical stress-strain behavior for ORNL foam before and after densification.

Densification by the SMJ process increases the thermal conductivity and density of graphitic foam while decreasing the thermal conductivity anisotropy associated with orientation. The thermal conductivity anisotropy of sample 180A (raw foam) was 1:2.61 while that of the densified sample 180B was 1:1.96. Similarly, for sample 185A (raw foam) the anisotropy was 1:2.84 while that of the densified sample 185B was 1:2.35. The added densification material appears to take on an isotropy ratio expected due to the elongation of the bubbles in the starting foams. Clearly, however, a heat treatment is required to open the pores after four infiltrations so that subsequent cycles can be effective.

The high conductivity of the densified foam makes it a very attractive thermal management material. Additionally, the densification has a significant impact on the compressive strength of the foam increasing it from approximately 2 MPa to over 7 MPa with a corresponding increase in density of 110 - 130%. With these improved strengths, the foams are more suitable for a wide range of applications where the raw foam cannot meet the stringent durability requirements, such as a finned heat sink for power electronics.

Status of Milestones

Milestone 1: Design, fabricate, and evaluate an improved heat sink for power electronics on microturbines utilizing graphite foam (September 1, 2004). New finned structure has been made and characterized as suitable for a finned structure. Next the design and construction phase will commence.

Industry Interactions

Work is about to begin with Unifin to start designing a finned heat sink for cooling power electronics.

Publications/Presentations

Submitted paper to:

Klett, J., S. Jones, L. Klett, and C. Walls. *High Thermal Conductivity Graphitic Foam Reinforced Carbon-Carbon Composites*. in *SAMPE® 2003 (48th ISSE)*, Long Beach, CA, (2003).

References

1. Klett, J., *High Thermal Conductivity, Mesophase Pitch-Derived Graphitic Foams.* Journal of Composites in Manufacturing, 15 (4), p. 1-7 (1999).
2. Ott, R., A. Zaltash, and J. Klett. *UTILIZATION OF A GRAPHITE FOAM RADIATOR ON A NATURAL GAS ENGINE-DRIVEN HEAT PUMP*. in *2002 ASME International Mechanical Engineering Congress & Exposition*, New Orleans, Louisiana,, (2002).
3. Wapner, P.G., W.P. Hoffman, and S. Jones, *Carbon and ceramic matrix composites fabricated by a rapid low-cost process incorporating in-situ polymerization of wetting monomers,* US Patent 6,309,703 (2001).

MATERIALS FOR ADVANCED RECIPROCATING ENGINES

Advanced Materials for Exhaust Components of Reciprocating Engines

P. J. Maziasz and N.D. Evans
Metals and Ceramics Division
Oak Ridge National Laboratory
P.O. Box 2008, Oak Ridge, TN 37831-6115
Phone: (865) 574-5082, E-mail: maziaszpj@ornl.gov

Objective

This program addresses the general high-temperature and performance limitations of various critical exhaust components (exhaust valve, exhaust manifold, turbocharger housing) for advanced natural gas reciprocating engine systems (ARES). For exhaust valves, advanced ARES engines are using Ni-based superalloys and pushing the temperatures up. For this component, this program is assessing the performance of current valves and coatings systems, and their potential for use at higher temperatures.

Highlights

ORNL is currently doing detailed microcharacterization of Ni-based superalloy valves provided by Waukesha Engine Division, Dresser Industries, Inc. and their component supplier, TRW Automotive Division, TRW, Inc. Significant changes in microstructure can be seen between fresh and engine-tested (without failure) valves, this quarter, analysis focuses on the interfaces between the basemetal and the coatings or weld-overlays.

Technical Progress

Nickel-based superalloys like Nimonic 80A, 90, Pyromet 31 and Waspaloy are used to make exhaust valves for a variety of advanced diesel and ARES engines. These valves can also have various weld-overlays on the face contacting the valve seat, or coatings on the face inside the combustion chamber. High-temperature engine exposure changes the base-metal microstructure and mechanical properties as well as the structure at the coating and base-metal interface.

ORNL is currently doing detailed microcharacterization of Ni-based superalloy valves provided by Waukesha Engine Division, Dresser Industries, Inc. and their component supplier, TRW Automotive Division, TRW, Inc. Significant changes in microstructure can be seen between fresh and engine-tested (without failure) valves, including grain structure and the various precipitate phases. Microcompositional analysis is being used to identify the various phases. This quarter, similar analysis is being focused on the interfaces between the base metal and the coatings or weld-overlays. After microcharacterization, hardness profiles will be used to correlate mechanical properties changes with the changes in microstructure.

Status of Milestones

FY 2003 – Complete characterization of TRW/Waukesha Ni-based superalloy valves to define changes during service and potential performance limitations. Identify metallurgical/weld-overlay or coating avenues for improved performance and reliability (May 2003) – on schedule.

Industry Interactions

Discussions continued with Waukesha Engine Dresser, Inc. (Joe Derra, Manager of Materials and Analysis) and TRW Engine Components (Victor Levin, Manager-Materials Engineering) about examining current exhaust valves with more severe engine exposure, and developing valves with improved performance. Non-disclosure agreement was signed and discussions about a joint CRADA project began.

Problems Encountered

None

Publications/Presentations

None

Development of Catalytically Selective Electrodes for NOx and Ammonia Sensors

Timothy R. Armstrong
Metals and Ceramics Division
Oak Ridge National Laboratory
P.O. Box 2008, Oak Ridge, TN 37831-6084
Phone: (865) 574-7996, E-mail: armstrongt@ornl.gov

Objective

To develop non-catalytic and catalytically selective electrodes for use in NOx and ammonia sensors and to build and test sensors using the materials and technology developed

Technical Highlights

We have developed a new Infrared test stand that will alloy rapid testing of multiple electrode materials in a single step. This test stand will measure the DT of the material based on the adsorption of the desired species on the electrode surface. This will allow rapid screening of numerous samples on a single test coupon. **First indications are that this should be a standard test for every sensor material where adsorption is the key sensing mechanism.**

Technical Progress

1. We have completed construction on a electrode test stands to screen a large number of potential NO sensitive materials. The test stand is composed of a high-temperature furnace, a gas mixing panel to mix CO, CO2, NO, NO_2, SO_2 and hydrcarbons, a chemiluinesence sensor to determine NO and NO_2 concentrations, and a meter to measure the EMF generated.

2. We have initiated Nox sensor testing using the new test facility. Initial studies we carried out on materials well documented in the literature. Results from these studies indicate that we were able to duplicate published values for EMF for both NO and NO2 on $ZnFeO_3$.

3. A new test has been designed to determine the ability of the catalyst to adsorb NO and NO_2. This test is based on infrared adsorption. A test stand has been designed with a quartz window through which an IR camera will focus on the catalysts deposited on an insulating body. The change in temperature of the catalyst when exposed can be measured with the IR camera. The greater the change in temperature the greater the ability of the catalyst to adsorb NO and NO_2. This method is being developed as a quick screen of new catalyst materials ad will be applied to NH_3 as well.

Status of Milestones

1. Determine kinetics of NO reaction on electrode as a function of temperature and environment.

It was found that this is a more complex phenomena that originally thought and will take more time than anticipated. This was the driver for the development of the IR sampling test stand. Because the reaction differs as the composition of the electrode or catalyst changes we need a method to rapidly screen, qualitatively and quantitatively, many samples. This new test stand will allow us to find those materials that sensor NO, NO_2, or NH_3 well and further develop their composition. We will also, using this test stand be able to see what exhaust gases interfere with the adsorption of the desired species.

2. Fabricate and test a prototype NOx sensor (09/03)

Due to the late start of this project and the dependence on the electrode material this will be delayed 1 year.

Industrial Interactions

We meet with members from DuPont sensor development group in December. They expressed interest in our work and would like to partner with us in the future. DuPont is developing sensors for diesel and gas fired reciprocating engines.

Problems Encountered

Funding to date has been exhausted

Publications/Presentations

None

Internal Distribution

B. L. Armstrong, 4515, MS-6063, armstrongbl@ornl.gov
T. R. Armstrong, 4508, MS-6084, armstrongt@ornl.gov
P. F. Becher, 4515, MS-6068, becherpf@ornl.gov
T. M. Besmann, 4515, MS-6063, besmanntm@ornl.gov
C. A. Blue, 4508, MS-6083, blueca@ornl.gov
M. A. Brown, 4500N, MS-6186, brownma@ornl.gov
M. K. Ferber, 4515, MS-6069, ferbermk@ornl.gov
J. A. Haynes, 4515, MS-6063, haynesa@ornl.gov
D. R. Johnson, 4515, MS-6066, johnsondr@ornl.gov
M. A. Karnitz, 4500N, MS-6186, karnitzma@ornl.gov
J. O. Kiggans, 4508, MS-6087, kiggansjojr@ornl.gov
J. W. Klett, 4508, MS-6087, klettjw@ornl.gov
E. Lara-Curzio, 4515, MS-6069, laracurzioe@ornl.gov
H. T. Lin, 4515, MS-6068, linh@ornl.gov
R. A. Lowden, 4515, MS-6063, lowdenra@ornl.gov
P. J. Maziasz, 4500S, MS-6115, maziaszpj@ornl.gov
K. L. More, 4515, MS-6064, morekl1@ornl.gov
R. D. Ott, 4515, MS-6083, ottr@ornl.gov
B. A. Pint, 4500S, MS-6156, pintba@ornl.gov
D. T. Rizy, 3147, MS-6070, rizydt@ornl.gov
D. P. Stinton, 4515, MS-6063, stintondp@ornl.gov
R. W. Swindeman, 4500S, MS-6155, swindemanrw@ornl.gov
T. N. Tiegs, 4508, MS-6087, tiegstn@ornl.gov
P. F. Tortorelli, 4500S, MS-6156, tortorellipf@ornl.gov
I. G. Wright, 4500S, MS-6157, wrightig@ornl.gov
A. Zaltash, 3147, MS-6070, zaltasha@ornl.gov

External Distribution

ALLISON ADVANCED DEVELOPMENT CO., 1100 Wilson Blvd., Suite 1450, Arlington, VA 22209
J. Miles, r.jeffrey.miles@allison.com

ALM SYSTEMS, INC, 1920 N Street, NW, Suite 750, Washington, DC 20036
M. Kalin, mkalin@ibek.com

ARGONNE NATIONAL LABORATORY, 9700 S. Cass Ave., Argonne, IL 60439-4838
W. Ellingson, ellingson@anl.gov
J. P. Singh, jpsingh@anl.gov

BATTELLE MEMORIAL INSTITUTE, 505 King Avenue, Columbus, OH 43201
D. Anson, ansond@battelle.org

BAYSIDE MATERIALS TECHNOLOGY, 21150 New Hampshire Ave., Brookville, MD 20833
D. Freitag, dfreitag@ix.netcom.com

BCS, INC., 5550 Sterrett Place, Suite 216, Columbia, MD 21044
D. Bartley, dbartley@bcs-hq.com

BOWMAN POWER, 20501 Ventura Boulevard #285, Woodland Hills, CA 91364
T. Davies, tdavies@bowmanpower.co.uk
T. Hynes, adh.bowmanpower@att.net
K. Mehrayin, kmehrayin@bowmanpower.co.uk
M. Newnham, mnewnham@bowmanpower.co.uk
D. Flaxington, dflaxington@bowmanpower.co.uk

CALIFORNIA ENERGY COMMISSION
A. Soinski, asoinski@energy.state.ca.us

CANNON-MUSKEGON CORP., Box 506, Muskegon, MI 49443-0506
J. Wahl, jwahl@canmkg.com

CAPSTONE TURBINE CORP., 6430 Independence Ave., Woodland Hills, CA 91367
P. Chancellor, pchancellor@capstoneturbine.com
K. Duggan, kduggan@capstoneturbine.com
M. Stewart, mstewart@capstoneturbine.com
J. Willis, jwillis@capstoneturbine.com
M. Rodrigues, mrodrigues@capstoneturbine.com
B. Treece, btreece@capstoneturbine.com

CLEMSON UNIVERSITY, South Carolina Institute for Energy Studies, 386-2, Clemson, SC 29634-5180
L. Golan, glawren@clemson.edu
R. Wenglarz, rwnglrz@clemson.edu
J. Hinson, jhinson@clemson.edu

CONNECTICUT RESERVE TECHNOLOGIES, 2997 Sussex Ct., Stow, OH 44224
E. Baker, baker@crtechnologies.com
S. Duffy, sduffy@crtechnologies.com
J. Palko, jpalko@crtechnologies.com

DTE ENERGY, 37849 Interchange Dr., Suite 100, Farmington Hills, MI 48335
M. Davis, davism@dteenergy.com

ELECTRIC POWER RESEARCH INSTITUTE, 3412 Hillview Ave., Palo Alto, CA 94303
J. Stringer, jstringe@epri.com

ELGILOY SPECIALTY METALS, 1565 Fleetwood Drive, Elgin, IL 60123
T. Bartel, terryb@elgiloy.com

ELLIOTT ENERGY SYSTEMS, 2901 S.E. Monroe Street, Stuart, FL 34997
D. Burnham, dburnham@elliott-turbo.com
D. Dewis, ddewis@elliott-turbo.com

ENERGETICS, INC., 501 School St., SW, Suite 500, Washington, DC 20024
R. Scheer, rscheer@energeticsinc.com

ENERGY TECHNOLOGIES APPLICATIONS, 5064 Camino Vista Lujo, San Diego, CA 92130-2849
T. Bornemisza, borneger@ix.netcom.com

GAS TURBINE ASSOCIATION, 1050 Thomas Jefferson St., NW, 5th Fl, Washington, DC 20007
J. Abboud, abboud@advocatesinc.com

GENERAL ELECTRIC (GE) CR&D, 1 Research Circle, Building K1-RM 3B4, Niskayuna, NY 12309
S. Correa, correa@crd.ge.com
K. Luthra, luthra@crd.ge.com
J. VanDerwerken, vanderwerken@crd.ge.com
C. Johnson, johnsonca@crd.ge.com

GENERAL ELECTRIC AIRCRAFT ENGINES, One Neumann Way, Mail Drop M89, Cincinnati, OH 45215-1988
R. Darolia, ram.darolia@ae.ge.com

GENERAL ELECTRIC POWER SYSTEMS, One River Rd., 55-127, Schenectady, NY 12345
R. Orenstein, robert.orenstein@ps.ge.com

GENERAL ELECTRIC POWER SYSTEMS, Gas Technology Center, 300 Garlington Road, Greenville, SC 29615
P. Monaghan, philip.monagham@ps.ge.com

HAYNES INTERNATIONAL, INC., 1020 W. Park Avenue, P.O. Box 9013, Kokomo, IN 46904-9013
V. Ishwar, vishwar@haynesintl.com
D. Klarstrom, dklarstrom@haynesintl.com

HONEYWELL CERAMIC COMPONENTS, 2525 W. 190th St., Torrance, CA 90504
D. Foley, dan.foley@honeywell.com
C. Li, chien-wei.li@honeywell.com
D. Newson, danielle.newson@honeywell.com
M. Savitz, MaxineSavitz@aol.com
J. Wimmer, jim.wimmer@honeywell.com
M. Mitchell, michele.mitchell@honeywell.com

HONEYWELL COMPOSITES, 1300 Marrows Rd., PO Box 9559, Newark, DE 19714-9559
R. Matsumoto, roger.matsumoto@honeywell.com

HONEYWELL ENGINES, SYSTEMS, & SERVICES 2739 E. Washington St., PO Box 5227, Phoenix, AZ 85010

B. Schenk, bjoern.schenk@honeywell.com
M. Masoudipour, mike.masoudipour@honeywell.com
HONEYWELL POWER SYSTEMS, 8725 Pan American Freeway NE, Albuquerque, NM 87113
S. Wright, e.scott.wright@honeywell.com

HOWMET RESEARCH CORP., 1500 South Warner St., Operhall Research Center, Whitehall, MI 49461-1895
B. Mueller, bmueller@howmet.com
R. Thompson, rthompson@howmet.com

INGERSOLL-RAND ENERGY SYSTEMS, 32 Exeter St., Portsmouth, NH 03801
A. Kaplau-Colan, alex_haplau-colan@ingersoll-rand.com
M. Krieger, michael_krieger@irco.com
J. Johnson, jay_johnson@ingersoll-rand.com
J. Kesseli, jim_kesseli@ingersoll-rand.com
J. Nash, jim_nash@ingersoll-rand.com

KENNAMETAL INC. 1600 Technology Way, P.O. Box 231, Latrobe, PA 15650-0231
R. Yeckley, Russ.yeckley@kennametal.com

KINECTRICS NORTH AMERICA, 124 Balch Springs Circle, SW, Leesburg, VA 20175
B. Morrison, blake.Morrison@kinectrics.com

KRUPP VDM TECHNOLOGIES CORP., 11210 Steeplecrest, Suite #120, Houston, TX 77065-4939
D. Agarwal, dcagarwal@pdq.net

NASA GLENN RESEARCH CENTER, 21000 Brookpark Rd., MS 49-7, Cleveland, OH 44135
D. Brewer, david.n.brewer@grc.nasa.gov
J. Gykenyesi, john.p.gyekenyesi@lerc.nasa.gov
S. Levine, stanley.r.levine@lerc.nasa.gov
N. Nemeth, noel.n.nemeth@grc.nasa.gov
B. Opila, opila@grc.nasa.gov

NATIONAL RURAL ELECTRIC COOPERATIVE ASSOC., 4301 Wilson Blvd., SS9-204, Arlington, VA 22203-1860
E. Torrero, ed.torrero@nreca.org

NATURAL RESOURCES CANADA, 1 Haanel Drive, Nepean, Ontario, Canada K1A 1M1
R. Brandon, rbrandon@nrcan.gc.ca

PCC AIRFOILS, INC., 25201 Chagrin Blvd., Suite 290, Beachwood, OH 44122
C. Kortovich, ckortovich@pccairfoils.com

PENN STATE UNIVERSITY, Applied Research Laboratory, PO Box 30, State College, PA 16823
J. Singh, jxs46@psu.edu

PRAXAIR SURFACE TECHNOLOGIES, 1500 Polco St., Indianapolis, IN 46224
R. Novak, richard_c_novak@praxair.com

RICHERSON AND ASSOC., 2093 E. Delmont Dr., Salt Lake City, UT 84117
D. Richerson, richersond@aol.com

ROLLS-ROYCE ALLISON, 2925 W. Minnesota St., PO Box 420, Indianapolis, IN 46241
S. Berenyi, steve.g.berenyi@allison.com
P. Heitman, peter.w.heitman@allison.com
F. Macri, francis.g.macri@allison.com

SAINT-GOBAIN CERAMICS & PLASTICS, INC., Goddard Road, Northboro, MA 01532
R. Licht, robert.h.licht@saint-gobain.com
M. Abouaf, Marc.Abouaf@saint-gobain.com
V. Pujari, Vimal.K.Pujari@saint-gobain.com

SEBESTYEN, T., Consultant, 6550 Mission Ridge, Traverse City, MI 49686-6123
T. Sebestyen, sebestyen@chartermi.net

SIEMENS WESTINGHOUSE POWER CORP., 1310 Beulah Rd., Pittsburgh, PA 15235-5098
M. Burke, michael.burke@swpc.siemens.com
C. Forbes, christian.forbes@swpc.siemens.com

SOLAR TURBINES, INC., TurboFab Facility, 16504 DeZavala Rd., Channelview, TX 77530
B. Harkins, harkins_bruce_d@solarturbines.com

SOLAR TURBINES INC., 818 Connecticut Ave., NW, Suite 600, Washington, DC 20006-2702
R. Brent, solardc@bellatlantic.net

SOLAR TURBINES, INC., 2200 Pacific Highway, PO Box 85376, MZ R, San Diego, CA 92186-5376
P. Browning, browning_paul_f@solarturbines.com
M. Fitzpatrick, fitzpatrick_mike_d@solarturbines.com
P. Montague, montague_preston_j@solarturbines.com
M Van Roode, van_roode_mark_x@solarturbines.com
M. Ward, ward_mike_e@solarturbines.com
J. Price, jeffprice@solarturbines.com

SOUTHERN CALIFORNIA EDISON COMPANY, 2244 Walnut Grove Avenue, Rosemead, CA 91770
S. Hamilton, hamiltsl@sce.com

SOUTHERN COMPANY, 600 N. 18th Street, 14N-8195, P.O. Box 2641, Birmingham, AL 35291
S. Wilson

STEVEN I. FREEDMAN, Engineering Consultant, 410 Carlisle Ave., Deerfield, IL 60015
S. Freedman, sifreedman@aol.com

STAMBLER ASSOCIATES, 205 South Beverly Drive, Suite 208, Beverly Hills, California 90212
I. Stambler

THE BOEING COMPANY, Rocketdyne Propulsion & Power, 6633 Canoga Avenue
MC: GB-19, P.O. Box 7922, Canoga Park, CA 91309-7922
G. Pelletier, gerard.pelletier@west.boeing.com

TELEDYNE CONTINENTAL MOTORS, 1330 W. Laskey Rd., PO Box 6971, Toledo, OH 43612-0971
J. T. Exley, texley@teledyne.com

TURBEC
L. Malmrup, lars.malmrup@turbec.com

UCI COMBUSTION LABORATORY, U. of CA, Irvine, Irvine, CA 92697-3550
V. McDonell, mcdonell@ucic1.uci.edu

UDRI, Ceramic & Glass Laboratories, 300 College Park Ave., Dayton, OH 45469-0172
A. Crasto, allan.crasto@udri.udayton.edu
G. Graves, gravesga@udri.udayton.edu
N. Osborne, osborne@udri.udayton.edu
R. Wills, roger.wills@udri.udayton.edu

UNITED TECHNOLOGIES RESEARCH CENTER, 411 Silver Lane MS 129-24, East Hartford, CT 06108
H. Eaton, eatonhe@utrc.utc.com
J. Holowczak, holowcje@utrc.utc.com
T. Rosfjord, rosfjotj@utrc.utc.com
J. Smeggil, smeggijg@utrc.utc.com
G. Linsey, linseygd@utrc.utc.com
J. Shi, shij@utrc.utc.com
E. Sun, suney@utrc.utc.com
D. Mosher, mosherda@utrc.utc.com

UNIVERSITY OF CALIFORNIA, Department of Mechanical Engineering, Berkeley, CA 94720
R. Dibble, rdibble@newton.berkeley.edu

UNIVERSITY OF MARYLAND, Department of Mechanical Engineering, College Park, MD 20742-3035
R. Radermacher, rader@eng.umd.edu

US DOE-NETL, P. O. Box 880, MSO-D01, 3610 Collins Ferry Rd., Morgantown, WV 26507-0880

C. Alsup, Jr., charles.alsup@netl.doe.gov
A. Layne, abbie.layne@netl.doe.gov
L. Wilson, lane.wilson@netl.doe.gov

US DOE-NETL, PO Box 10940, Pittsburgh, PA 15236
N. Holcombe, norman.holcombe@netl.doe.gov
U. Rao, rao@netl.doe.gov
US DOE CHICAGO OPERATIONS OFFICE, 9800 S. Cass Ave., Argonne, IL 60439
J. Jonkouski, jill.jonkouski@ch.doe.gov
J. Mavec, joseph.mavec@ch.doe.gov
J. Livengood, joanna.livengood@ch.doe.gov
S. Waslo, stephen.waslo@ch.doe.gov

US DOE-HQ, 1000 Independence Ave., S.W., Washington DC 20585
R. Fiskum, ronald.fiskum@ee.doe.gov
D. Haught, debbie.haught@ee.doe.gov
P. Hoffman, patricia.hoffman@ee.doe.gov
W. Parks, william.parks@ee.doe.gov
M. Smith, merrill.smith@ee.doe.gov
C. Sorrell, charles.sorrell@ee.doe.gov

WILLIAMS INTERNATIONAL, 2280 West Maple Rd., PO Box 200, Walled Lake, MI 48390-0200
G. Cruzen, g.cruzen@williams-int.com
W. Fohey, w.fohey@williams-int.com
C. Schiller, cschiller@williams-int.com

WRIGHT PATTERSON AIRFORCE BASE,
R. Sikorski, ruth.sikorski@wpafb.af.mil